• U C •

FCTUC FACULDADE DE CIÊNCIAS
E TECNOLOGIA
UNIVERSIDADE DE COIMBRA

Daniela Filipa Dias Martins

Gaussianization methods for structural brain imaging

Coimbra, julho 2014

• U C •

FCTUC FACULDADE DE CIÊNCIAS
E TECNOLOGIA
UNIVERSIDADE DE COIMBRA

Daniela Filipa Dias Martins

Gaussianization methods for structural brain imaging

Dissertação apresentada à Universidade de Coimbra para cumprimento dos requisitos necessários à obtenção do grau de Mestre em Engenharia Biomédica.

Orientador:
Dr. João M. S. Pereira

Coimbra, julho 2014

Este trabalho foi desenvolvido em colaboração com:

IBILI

Faculdade de Medicina da Universidade de Coimbra

Acknowledgements

Ao longo de todo o meu percurso académico várias foram as pessoas que contribuíram para o meu crescimento e sucesso e, por isso, não podia deixar de guardar umas palavras de sinceros agradecimentos.

Em primeiro lugar, queria dedicar um especial agradecimento ao meu orientador, o Dr. João Pereira, pela total disponibilidade, dedicação e compreensão ao longo deste último ano e ainda pela confiança depositada em mim. Quero também agradecer ao Dr. Miguel Patrício pela ajuda prestada sempre que necessário. Ao IBILI, e em especial ao Prof. Dr. Miguel Castelo-Branco por tornar possível a realização das teses de mestrado nesta instituição. Quero também deixar um obrigado ao Prof. Dr. Miguel Morgado, pois sem ele o curso de Engenharia Biomédica não seria o mesmo.

Não posso deixar de agradecer aos meus colegas mestrandos, em especial ao Fábio, por toda a ajuda e companheirismo prestados ao longo deste último ano.

Aos meus colegas de curso, principalmente às minhas amigas que sempre me acompanharam e apoiaram durante estes 5 anos. Queria deixar um agradecimento especial à Sofia, por toda a ajuda e compreensão que me tem demonstrado e por ter sido a melhor companhia desde o início desta vida académica; à Diana, por estar sempre presente nos bons e nos maus momentos e por ter sempre uma palavra de motivação para dar; à Carolina, à Patrícia, à Joana, à Marta, à Miriam e à Sara um muito obrigada!

Quero deixar um especial agradecimento ao Carlos, que sempre me apoiou e acreditou no meu sucesso, pela muita paciência que teve e pela ajuda que me deu, principalmente neste último ano e nesta última etapa de conclusão do curso.

Por último, deixo os meus sinceros agradecimentos, os mais importantes de todos, à minha família: em especial à minha irmã, que sempre esteve presente e que é o meu pilar, nunca me deixou ir abaixo e sempre me fez acreditar de que era capaz; aos meus queridos pais, por todo o apoio, confiança e dedicação, sem eles nada disto teria sido possível e, por isso, muito obrigada!

Resumo

A Neuroimagem, nomeadamente a estrutural, constitui uma vasta área de estudo atualmente, uma vez que permite o diagnóstico de doenças neurodegenerativas através de técnicas de imagiologia da estrutura do cérebro, nomeadamente através da Imagem por Ressonância Magnética.

O método usado neste trabalho para efeitos de análises morfométricas da estrutura do cérebro foi o *Voxel-Based Morphometry* (VBM), que tem como resultado final um mapa de parâmetros estatísticos que permite inferir sobre a existência de alterações a nível do volume de matéria cinzenta, comparando um grupo de sujeitos controlo com um grupo de sujeitos com alguma patologia que possa estar associada a atrofia cerebral. A implementação desta técnica implica o registo das imagens de diferentes sujeitos e da respetiva segmentação para extração da matéria cinzenta, relevante para a análise. Os resultantes segmentos registados de matéria cinzenta têm de ser suavizados de modo a garantir a distribuição Gaussiana dos voxels das imagens, para que os testes estatísticos paramétricos posteriores sejam válidos. O método *standard* de Gaussianização baseia-se numa suavização que "esborrata" as imagens, diminuindo a capacidade do VBM para detetar pequenas regiões cerebrais afetadas, perdendo resolução e especificidade anatómica. Surge assim a necessidade de desenvolver técnicas alternativas de Gaussianização, o objetivo deste trabalho.

Para este efeito, foram desenvolvidos dois métodos principais: i) um baseado na manipulação dos histogramas das imagens; e ii) outro baseado na deformação Gaussiana das imagens. Todos os métodos foram implementados em Matlab. A avaliação da normalidade foi efetuada por análise de resíduos resultantes da aplicação do modelo linear geral, e o impacto regional e visual foi realizado com base em análises VBM com sujeitos em que as regiões atróficas reais eram conhecidas.

Verificou-se que, em geral, os métodos desenvolvidos apresentaram resultados positivos tanto a nível de Gaussianização dos dados como a nível de precisão anatómica dos mapas estatísticos finais quando comparados com os métodos atualmente em uso, ainda que o uso de máscaras relativas tenha limitado a

comparabilidade dos métodos. Esta questão, bem como a avaliação quantitativa da preservação da anatomia conseguida pelos novos métodos, deve ser analisada em trabalho futuro.

Palavras-chave: Ressonância Magnética, Gaussianização, Voxel-Based Morphometry, Matéria Cinzenta.

Abstract

Neuroimaging, namely the structural, is a vast area of study currently, since it allows the diagnosis of neurodegenerative diseases by imaging of the brain structure, notably by Magnetic Resonance Imaging.

The method used in this work for the purpose of morphometric analysis of brain structure was Voxel-based Morphometry (VBM), whose final result is a map of statistical parameters that allows to infer about the existence of changes in grey matter volume, comparing a group of control subjects with a group of subjects with a condition that might be associated to brain atrophy. The implementation of this technique involves the registration of images from different subjects to a template and the respective segmentation for grey matter extraction, relevant to the analysis. The resulting grey matter registered segments must be smoothed to ensure Gaussian distribution of the voxels of the images, for the subsequent parametric statistical tests to be valid. The standard method of Gaussianization is based on an approach that "blurs" the images, decreasing the VBM's ability to detect small brain regions affected and thus losing anatomical resolution and specificity. This raises the need to develop alternative Gaussianization techniques, the goal of this work.

For this purpose, two main methods have been developed: i) one based on histogram manipulation of images; and ii) the other based on the Gaussian deformation of the images. All methods were implemented in Matlab. The assessment of normality was performed by analysis of the residuals resulting from the application of the general linear model, and the regional and visual impact assessment was based on VBM analyses with subjects where the atrophic regions were known.

It was found that, in general, the developed methods showed positive results both in terms of data Gaussianization as in anatomical accuracy of the final statistical maps, when compared with the methods currently in use. The use of relative masks has limited the comparability of the methods though – this matter, along with the definition of an objective metric for anatomical detail preservation, should be the focus of future work.

Key-words: Magnetic Resonance, Gaussianization, Voxel-Based Morphometry, Grey Matter.

List of figures

List of tables

List of Abbreviations

CDF	Cumulative Density Function
CLT	Central Limit Theorem
CSF	Cerebrospinal Fluid
FID	Free Induction Decay
fMRI	Functional Magnetic Resonance Imaging
FT	Fourier Transform
FWE	Family-Wise Error
FWHM	Full Width at Half Maximum
GLM	General Linear Model
GM	Grey Matter
ICBM	International Consortium for Brain Mapping
MNI	Montreal Neurological Institute
MRI	Magnetic Resonance Imaging
NMR	Nuclear Magnetic Resonance
PDF	Probability Density Function
RF	Radiofrequency
ROI	Region of Interest
SNR	Signal-to-Noise Ratio
TGMV	Total Grey Matter Volume
VBM	Voxel-Based Morphometry
WM	White Matter

List of symbols

$\boldsymbol{\mu}$	Magnetic moment
$\mathbf{B}_0$	External magnetic field
$\mathbf{M}_0$	Macroscopic magnetization
$\mathbf{M}_T$	Transverse magnetization
$\mathbf{M}_L$	Longitudinal magnetization
ω_L	Larmor frequency
γ	Gyromagnetic ratio
$\mathbf{B}_1$	External magnetic field
τ	Duration of the radio frequency pulse
θ	Flip angle
T_1	Longitudinal relaxation time
T_2	Transverse relaxation time
T_R	Repetition time
T_E	Echo time
Ig	Greatest multiple of grey matter probability and tissue contraction
σ	Standard deviation
y	Observed value for the general linear model
$\boldsymbol{\beta}$	Vector of regressor variables for the general linear model
$\mathbf{X}$	Vector of parameters for the general linear model
$\boldsymbol{\varepsilon}$	Error term
$\mathbf{I}_S$	Smoothed image
$\mathbf{I}$	Original image
$\mathbf{x}'$, $\boldsymbol{\tau}$	Coordinates
$\mathbf{G}$	Convolution function
r	Grey levels of an image

T	Transformation function
s	Grey levels of the transformed image
T^{-1}	Inverse transformation function
$p_r(r)$	Probability density function of the variable r
$p_s(s)$	Probability density function of the variable s
ω	Dummy variable of integration
$p_r(r_k)$	Probability of occurrence of a grey level r_k
n_k	Number of pixels with level r_k
L	Total number of possible levels
p	Probability value
α	Scale factor representing the maximum norm of the deformation vectors
I	Intensity values
$\mathbf{x'}$	Arbitrary position of a coordinate
$\mathbf{x_1}$, $\mathbf{x_2}$	Gradient neighbours of $\mathbf{x'}$
ω	Normalized Euclidean distance between $\mathbf{x'}$ and $\mathbf{x_1}$
$I(\mathbf{x})$	Image intensity at location $\mathbf{x}$
r_Q	Correlation coefficient of the QQ plot
x_1, x_2, x_n	n observations of the model residuals
q_1, q_2, q_n	Distribution quantiles of the model residuals
X, Y, Z	3D coordinate arrays
ax, ay, az	Dimensions of the original image
$\mathbf{Y}$	Matrix containing the intensities values of the grey matter segment
$\boldsymbol{\beta_1, \beta_2, \beta_3}$	Regressors of the general linear model
n	number of iterations

Contents

Chapter 1

1 INTRODUCTION

Neuroimaging is a widely studied field of research that uses multiple techniques to image the structure as well as the function/activity of the brain. It can be divided in two broad categories: i) structural imaging, dealing with the structure of the brain and the diagnosis of neurodegenerative diseases and injury, for instance, leaning mostly on Magnetic Resonance Imaging (MRI); ii) functional imaging, notably functional MRI (fMRI), which provides invaluable information about the synaptic activity of the brain through measures of blood oxygenation [1] . The current thesis will only focus on structural MRI, notably on brain Morphometry analyses.

Morphometry is the study of changes in the shape and volume structures. To perform Morphometry analyses in the brain, and thus evaluate the changes observed in the structural MRI images, two key methods stand out: i) region of interest (ROI) analyses, and ii) voxel-based Morphometry (VBM). A region of interest can be defined as a particular anatomical region of the brain, chosen according to a specific a priori hypothesis on where the alteration should be found. The use of ROIs can be advantageous because they can reduce the Type I error, diminishing the occurrence of false positives by limiting the number of statistical tests to a few ROIs [2]. Nonetheless, their selection process can lead to important biases in the analyses by casting out all other parts of the brain; moreover, ROIs should ideally be manually drawn, which is very time consuming and requires complicated logistics, and the automated solutions may be prone to errors. In order to bypass these fundamental barriers, while taking into account that the gold standard is indeed the manual ROI method, used as a tie-breaker whenever is required, the preferred whole brain analysis automated method is VBM.

VBM is a neuroimaging technique that, after pre-processing the MRI scans, creates statistical parametric maps to infer on changes pertaining to brain parenchyma, notably grey matter: this allows for the identification of differences between

+groups (e.g. atrophy [3]) or neural correlates of e.g. a given test score [4]. In brief, this procedure involves the spatial normalization of all brains to the same standard space [5], known as template, in order to ensure that the voxels that are being compared correspond to the same area of the brain. This is followed by the segmentation of the brain into different tissue types: grey matter (GM), white matter (WM) and cerebrospinal fluid (CSF), the focus being mostly on GM [5] [3]. The resulting tissue-specific segments are then smoothed, whereby the intensity of each voxel is replaced by the weighted average of the surrounding voxels, rendering the data normally distributed in the process [6]. This step is performed by using a three-dimensional (3D) Gaussian kernel that is characterized by its dispersion, as measured by the Full Width at Half Maximum (FWHM) [3]. The smoothed images are then submitted to statistical parametric t-tests, via implementation of the general linear model (GLM) to detect significance areas that reveal tissue changes. The resulting output is a statistical parametric map, highlighting regions of significant differences and/or correlations, also known as 'glass brain' [3].

This thesis will focus on the smoothing step of the process described above. This step ensures a fundamental pre-requisite for parametric statistical analyses, which is the normality of the data. Furthermore, this Gaussianization also compensates for possible inaccuracies that may occur from the registration step, while also increasing the signal-to-noise ratio (SNR), thus reducing the variance across subjects and making the statistical analysis more sensitive. However, this "blurring" of the images usually diminishes the ability to accurately locate significant regions in brain [3], resulting in a loss of important anatomical information and compromising the validity of this technique. As such, there is a clear motivation to explore the use of alternative techniques for smoothing. The point of this work is to attempt to ensure normality of the data by using non-blurring or less blurring methods than the standard Gaussian kernel approach.

In summary, the current work has three main goals:

i) implement a method for the assessment of the normality of the data, both globally and by mapping out locations of "difficult" Gaussianization;

ii) develop and assess alternative methods of Gaussianization that could address the drawbacks of the smoothing method currently used, comparing these to the standard approach; and

iii) visually assess the resulting statistical maps to evaluate anatomical accuracy gains, if any.

Chapter 2

2 THEORETICAL INTRODUCTION

2.1 Magnetic Resonance Imaging

Magnetic Resonance Imaging is a medical imaging technique used to investigate the anatomy or function of the brain. It is based on the phenomenon of nuclear magnetic resonance (NMR): in the presence of an external magnetic field, and when a radiofrequency (RF) pulse is applied, particular nuclei suffer excitation followed by relaxation when the RF stimulus is removed. There are many nuclei that show that capability: because of the large concentration in the human body, hydrogen nuclei (H^1) are the ones used in magnetic resonance essays [7].

The nuclei have some magnetic properties that are essential to the occurrence of the NMR phenomenon, namely angular moment or spin as well as an associated magnetic moment $\boldsymbol{\mu}$: as such these nuclei can be seen as behaving like tiny magnets, spinning around their axis. In the absence of an external magnetic field, the magnetic moments of all the nuclei will cancel each other out, as their orientations are arbitrarily aligned in space.

Under the effect of an external magnetic field $\mathbf{B}_0$, defining the longitudinal direction, the moments of the nuclei will align with this field [8]. While the individual spins of all the nuclei have different orientations, the macroscopic magnetization $\mathbf{M}_0$, resulting from the superimposition of all the magnetic moments, in equilibrium, will have the same orientation as the external magnetic field [7]. Thus, the transverse magnetization $\mathbf{M}_T$ will be zero but the longitudinal magnetization $\mathbf{M}_L$ will be equal to $\mathbf{M}_0$. As seen in Figure 2.1, the aligned spins will continue to precess, albeit this time along the longitudinal axis. This precession will have a specific angular frequency, called the Larmor frequency:

$$\omega_L = \gamma B_0 \qquad \textbf{(2-1)}$$

where B_0 is the intensity of the external magnetic field (measured in Tesla) and γ is the gyromagnetic ratio, which depends on the nuclear species.

To have a measurable signal, however, the magnetization as to be forced to flip towards the transversal plane, where the receiving coils are while read the magnetization. In order to do that, another external magnetic field $\mathbf{B}_1$ is needed. $\mathbf{B}_1$ is applied perpendicularly to $\mathbf{B}_0$, forcing the spins to rotate towards it if the frequency of this new field is that of the resonance of the system: as a result the magnetization $\mathbf{M}_0$ will start to precess around $\mathbf{B}_1$ [7](see Figure 2.1 b).

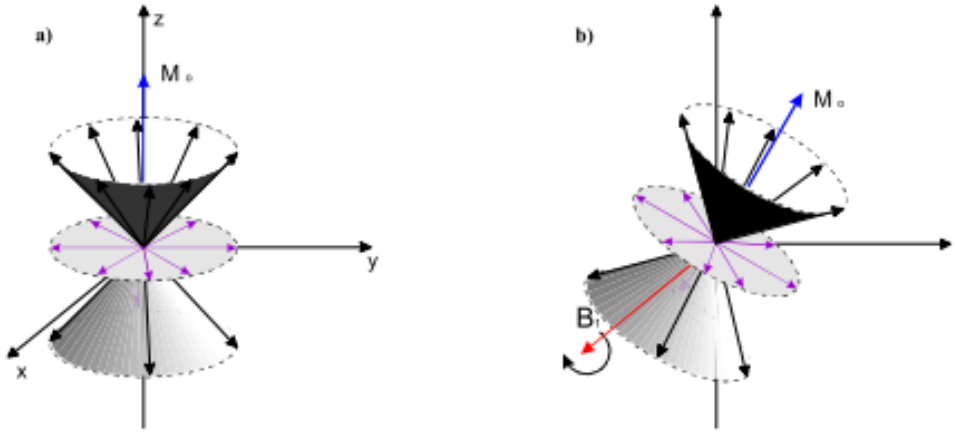

Figure 2.1 – a) magnetization $\mathbf{M}_0$ at equilibrium; b) magnetization $\mathbf{M}_0$ after the application of the RF field $\mathbf{B}_1$ **[7]**.

To observe an effect, the frequency of the second field has to be exactly equal to the Larmor frequency, which is why this is a resonance phenomenon. Given the usual field strengths (1.5T and 3T in the clinic), combined with the gyromagnetic constant associated with the hydrogen, the usual frequency used is in the RF range [7].

When the $\mathbf{B}_1$ generating RF pulse is turned off, the magnetization M_0 will go back to its original equilibrium state along $\mathbf{B}_0$. If the RF pulse has duration of τ seconds, $\mathbf{M}_0$ would have flipped towards $\mathbf{B}_1$ by a flip angle θ:

$$\theta = \omega\tau = \gamma B_1 \tau \qquad \textbf{(2-2)}$$

After the RF pulse is removed, it is observed that the magnetization components $\mathbf{M}_L$ and $\mathbf{M}_T$ return to their equilibrium values, releasing the absorbed energy, with characteristic time constants T_1 and T_2, known as longitudinal and transversal relaxation times, respectively. Typical values of T_1 and T_2 are 300 to 600 ms and 30 to 80 ms, respectively, and they depend on the nuclear species and on the chemical composition of the tissue [8].

Assuming that at a time t=0, $M_L(0) = 0$ and $M_T(0) = M_0$, the evolution of the amplitude for each magnetization is as shown in Figure 2.2. This phenomenon will be further expanded on below.

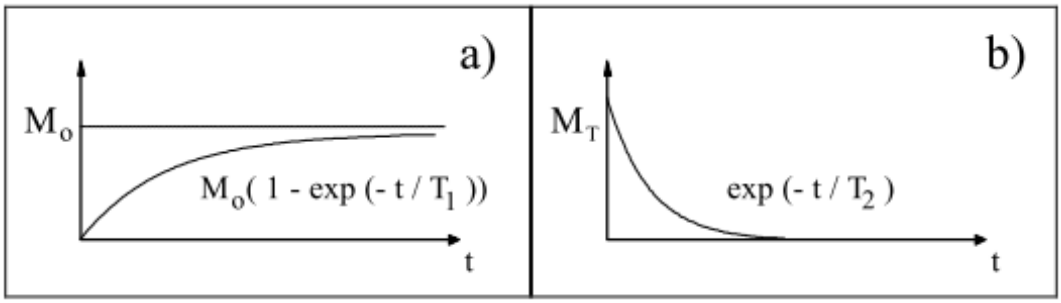

Figure 2.2 – a) evolution of the longitudinal component of the magnetization in time; b) evolution of the transversal component of the magnetization in time **[7]**.

2.1.1 Free Induction Decay signal

To summarize, one can say that the NMR phenomenon is characterized by an excitation pulse, causing the magnetization to flip by an angle θ, precessing around the z-axis with the frequency ω_L. As such, the picture shown in Figure 2.2 is not complete, as it ignores the characteristic oscillation of the system. In fact, the detected signal will also oscillate with ω_L and will fall off exponentially [7]:

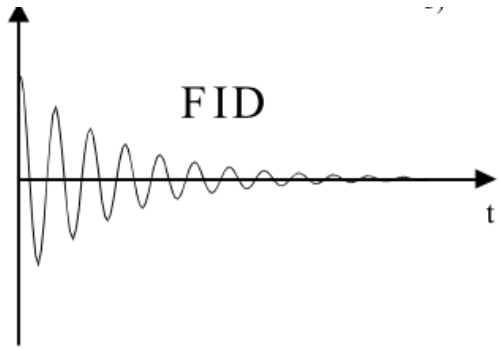

Figure 2.3 – Free Induction Decay signal.

This signal is called the *Free Induction Decay* (FID) signal and its amplitude is proportional to the nuclear magnetization and thus of the amount (density) of the protons in the tissue [8]. The decay is defined by the relaxation of the spins, as described above (Figure 2.3).

2.1.2 Relaxation Mechanisms

After an excitation with a 90^o RF pulse (it will be assumed that the flip angle will be 90^o for simplicity of representation, but it can be different) all the magnetization is oriented in the transverse direction and the individual nuclear moments **μ** are precessing in phase with each other. At this point, the longitudinal magnetization is equal to 0. However, after the removal of the RF pulse, $\mathbf{M}_L$ will re-grow and revert to its equilibrium state. This relaxation step is divided into two different processes that happen simultaneously: i) longitudinal or T_1 relaxation, which corresponds to longitudinal magnetization recovery; ii) transverse or T_2 relaxation, which corresponds to transverse magnetization decay [8]. This relaxation process gives information about the environment of the nuclei during a FID as it depends on time constants that are related to the characteristics of the tissue.

In the T_1 relaxation, the spins with added energy given by excitation will release that energy excess to their surroundings, the *lattice,* hence the designation of spin-lattice relaxation [7]. This recovery of the longitudinal magnetization follows an exponential curve and its recovery rate, T_1, is a tissue-specific time constant [9].

The transverse relaxation results from the misalignment of the spins. As they move together, the magnetic fields of the spins interact randomly, slightly modifying their precession rate. Because this process is caused by the interaction between spins, it is also called spin-spin relaxation [9]. As with the recovery rate T_1, the decay rate T_2 is also a tissue-specific time constant. Given the phase cancellation nature of this process, T_2 decay is always faster than T_1 recovery.

2.1.3 Data acquisition and image formation

The information obtained from an MR image is based on the macroscopic magnetization $\mathbf{M}_0$, which is proportional to the proton concentration in the tissue. However, the information about the location of the protons in the tissue is not present in the FID signal. This spatial information is essential to form an image. To map the volume excited in the tissue spatial encoding is needed. This is achieved through three steps: slice selection, phase encoding and frequency encoding [8], using spatial magnetic gradients in the three orthogonal directions.

In the slice selection step, a magnetic gradient is applied through the direction of the main magnetic field (z-axis), leading to a spatial variation of the magnetic field. Thus, each nucleus will have a frequency dependent on its position and it is possible to selectively excite a thin slice of the sample being imaged. The phase and frequency encoding of the spins are used to obtain the information of a single point (voxel, in 3D). This is achieved by applying two additional gradients. One temporary gradient is applied along the y-axis between the RF pulse and the readout, leading to a shift in the phase of the nuclei: by varying the duration of the gradient, one can have signals with different phase encodings. To have the frequency encoding, one third gradient is applied (along the x-axis) during the readout signal, allowing to identify pixels within the same phase encoding. As a result, the pixels with the same phase shift will have the same resonance frequency shift. With these two encodings, one can have 2D information, which is stored in k-space (Fourier space): each row has the information about the frequency (x-axis) and each column has the information about the phase (y-axis). The image is then built by calculating the 2D inverse Fourier Transform (FT) of the samples in the k-space [10]. The slice selection gradient allows for 3D information, applying the same method but in three dimensions.

2.1.4 Contrast images: T_1 and T_2

Resonant Magnetic Imaging allows the creation of contrast images in order to identify different areas in the tissue, and the presence of pathology. This is possible

because different tissues have different values of T_1 and T_2 and, in case of disease, these values may be especially altered.

In order to better explore this difference in time constants, MR images are acquired with specific pulse gradient sequences, called acquisition sequences. Insofar as they control the timing of the RF pulses, they are mainly characterized by two variables: i) repetition time (T_R), which is the time between two excitation pulses; and ii) echo time (T_E), the time between the RF pulse and the maximum of the spin echo, corresponding to the signal sampling [9].

The contrast T_1 is achieved by varying the repetition time while keeping T_E low to avoid contamination from T_2 relaxation. Considering a region A with low T_1 and a region B with high T_1: if T_R is much higher than both T_1's, the two regions will have time to completely recover their equilibrium state of magnetization and thus no contrast will be observed. However, if T_R is reduced to a value between the two T_1, region A will recover its longitudinal magnetization but the same will not happen with region B. This will lead to decrease in the signal from region B and consequently a decrease in its brightness in the image.

Analogously, considering two regions, with different T_2, to obtain a T_2 contrast, one should use an echo time higher than the lowest T_2 and lower than the highest T_2. That way, the transverse magnetization in the region with the highest T_2 will not decay, hence the detected signal derived from it will not decrease as much as the signal from the region with the lowest T_2 and the correspondent image will have greater brightness [8]. All the while, T_R should be kept high do dilute any contribution from T_1 relaxation.

In this work, it will only be considered the T_1 contrast images.

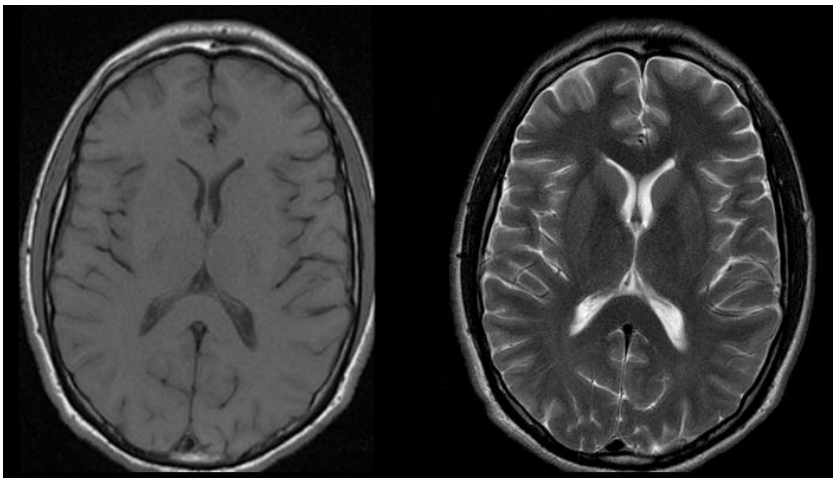

Figure 2.4 – Axial MRI. T_1 contrast (left) and T_2 contrast (right).

2.2 Voxel-Based Morphometry

A number of pathologies lead to subtle changes in the grey matter structure of the brain, although these may elude the human eye [10] [11]. In order to assess such patterns of structural change, structural MRI images can be used - notably T_1, given its high anatomical contrast - and the volume of certain brain regions, called regions of interest, can be extracted. Such an approach, however, fails to assess the overall brain structure and, by design, presents regional bias. Furthermore, the current gold standard for such an analysis is to manually delineate the regions, which is very time consuming and prone to errors; automatic ROI detection is currently gaining momentum, but it is still prone to errors [12]. An alternative is to use whole brain automated morphometry methods, notably Voxel-Based Morphometry, which allows us to localize regions of volumetric differences in brain tissue, notably in grey matter.

Voxel-Based Morphometry is therefore a neuroimaging analysis technique based on statistics to identify differences in the anatomy of the brain between different groups of subjects, or correlated with a given score, notably allowing for inferences about the presence of atrophy. For the purposes of this thesis, the focus will solely lie on the comparison between groups for the detection of grey matter atrophy.

In brief, MR scans are processed and analysed to produce statistical maps of changes in grey matter volume, comparing a group of subjects known as healthy (control) with a group of subjects with a pathology that may lead to cortical

atrophy [5]. This is a whole brain analysis and thus requires a coordinate by coordinate approach, i.e., it performs a voxel-by-voxel comparison, implying that the subjects in each groups must share the same (stereotactic) space: this is achieved by the first step of spatial normalization (registration), whereby all brains are fitted onto a standard template. Further to this step, in order to ensure that the analysis is only focused on the relevant parenchyma, the scans are segmented into different types of tissues in order to extract the grey matter. After this, the resulting grey matter segments are smoothed for statistical reasons and fed to a statistical model, using t-tests to produce statistical parametric maps of regions of significance (Figure 2.5).

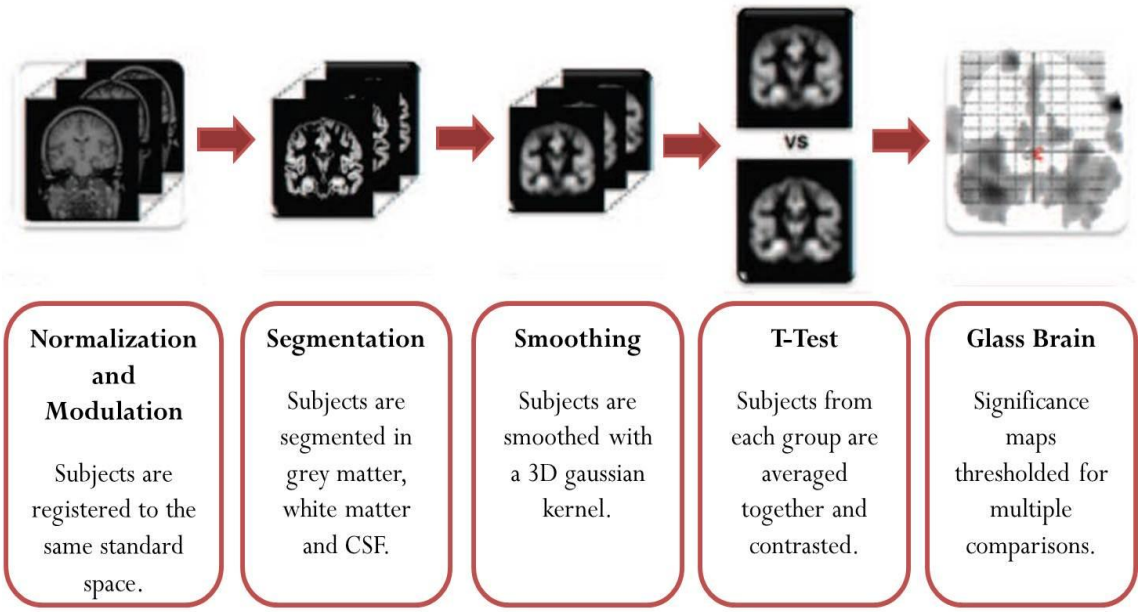

Figure 2.5 – VBM method.

Although this method is simple and is known to produce reliable results [5], as with any fully automated method the results must be analysed with caution as errors could have been introduced due to poor registration or segmentation, for instance [3].

The steps to perform a VBM analysis are described below in greater detail.

2.2.1 Spatial Normalization

The spatial normalization step consists in registering all the brains in the study onto the same template image, so that they can share the same stereotactic space, thus ensuring that the subsequent statistical comparison is comparing like for like, i.e. any given coordinate in any brain will correspond to the same structure across all brains [5]. The registration step is not an easy task because of the anatomy and the position of the brains varies across subjects, and a perfect solution is often not attainable or even biologically plausible [3].

Given a template that defines the standard space, usually a variant of the Montreal Neurological Institute (MNI) 305 or the International Consortium for Brain Mapping (ICBM) 152, each brain needs to be fitted onto it. In order to achieve this, the registration is usually performed in two steps: i) first a linear registration is performed in order to remove global differences between the subject and the template: this implies the estimation and application the optimum 12-parameter affine transformation [5]; ii) after the global differences are accounted for, as all brains are different at a small scale, minute differences are dealt with by performing a nonlinear registration in a local scale.

It is important that the quality of the registration is as high as possible and that the choice of the template is adequate to ensure an unbiased result [5]. The template used in the normalization step can be one specific MRI scan or the average of several MRI scans that have been registered in the same space, as both examples above are.

2.2.2 Modulation

When the registration step is performed, both linearly and non-linearly, expansions or contractions in regions do not affect the intensities of the voxels involved: if the size of a certain region decreases due to the normalization, the number of the corresponding voxels also decreases in the same proportion, but the image intensity remains the same. Thus, the information regarding the absolute tissue volume is not preserved. To solve this problem, each voxel of the image is multiplied by the local volume change given by the determinant of the Jacobian of

the corresponding spatial transformation [10]. Because this determinant quantifies the scaling applied during the registration on a given voxel, structures that were compressed will have a brighter intensity and the ones that were expanded to fit the template, pointing towards the presence of atrophy, will be dimmer. This happens both at a global and a local level - the former modulation needs to be controlled through a nuisance variable related to the size of the head, which will be explained below.

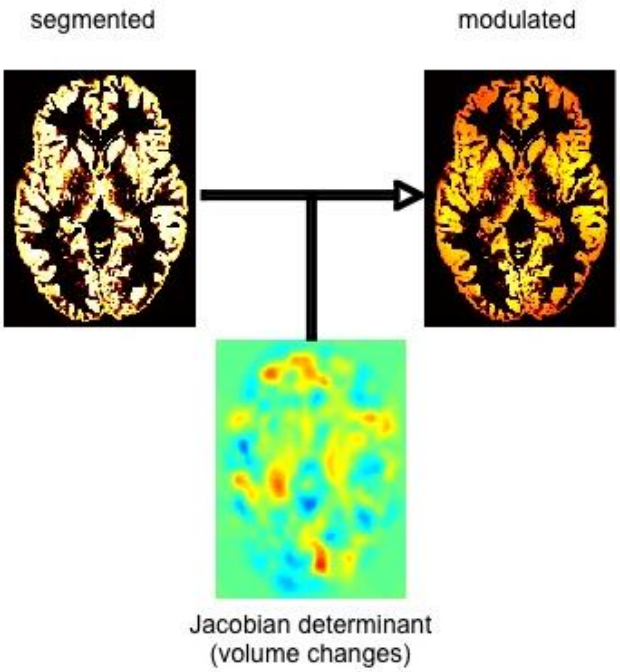

Figure 2.6 – Effect of modulating segmented images. The Jacobian determinant in the centre represents the volume changes due to non-linear registration [13].

2.2.3 Segmentation

The segmentation step enables the partition of the brain into different tissue types, notably into grey matter, white matter, cerebrospinal fluid and non-brain elements (Figure .2.7). This segmentation takes into account prior probability maps of healthy brain tissue and voxel intensities to produce *a posteriori* maps of probability distribution to classify the tissue, with values between 0 and 1 (probability of a given voxel belonging to a certain tissue type given its location and intensity): the resulting image will therefore be a probability map, with intensities proportional to the amount of grey matter in a given location [3].

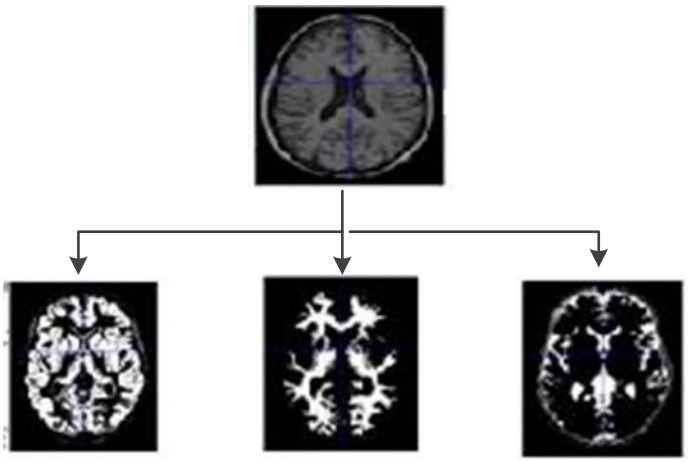

Figure .2.7 – Segmentation of the brain into grey matter (bottom right), white matter (bottom middle) and cerebrospinal fluid (bottom left).

In SPM8 (http://www.fil.ion.ucl.ac.uk/spm/), the software used in this thesis, this segmentation step is done simultaneously with the registration and modulation in what is called the unified segmentation [14]. This is done because, given a segmentation approach that uses *a priori* probability maps in standard space, both registration and segmentation are intrinsically dependent on each other. Moreover, the modulation is applied directly onto the resulting probability maps, which will no longer have a 0 to 1 scale, but rather a 0 to *Ig* scale, where *Ig* is a positive number corresponding to the greatest multiple of GM probability and tissue contraction. This is useful insofar as the intensity of the resulting segment reflects not only the probability of being grey matter but also the structural changes of the underlying structure: the intensity of each voxel is therefore proportional to a broader metric of GM volume.

2.2.4 Smoothing

Before performing the statistical analysis, the registered, modulated and segmented images are smoothed. This smoothing is achieved by the convolution of the image with a 3D isotropic Gaussian kernel, which is characterized by its full width at half maximum and it is related to the corresponding standard deviation σ as per the following relationship:

$$FWHM = \sqrt{8ln2} \cdot \sigma \quad \textbf{(2-3)}$$

The segments, as seen before, have intensity values between 0 and *I*, with most of the values near the extremities, which means that the data does not have a normal distribution. This is a fundamental prerequisite for the use of parametric statistical tests, which are easy to implement and very sensitive. Thus, the smoothing process ensures that each voxel covers the weighted average of the information contained in the surrounding tissue, rendering the data normally distributed by appealing to the Central Limit Theorem. Hence, since the data have a Gaussian distribution, the smoothing increases the validity of the statistical parametric tests while also reducing intersubject variability, which may be a remnant of the registration process [5].

The smoothing step has also other advantages, such as to increase the SNR, making the statistical analyses more sensitive. Furthermore, if the FWHM of the kernel is comparable to the size of the differences to be measured, the statistical tests will also be more accurate. However, excessive smoothing could reduce the ability of the method to localize changes in brain [3].

2.2.5 Statistical Analysis

The smoothed images are then averaged together and contrasted. The aim of the statistical analysis is to detect significant anatomical differences between the two groups of scans under study. This statistical significance is related to a p-value, which can be defined as the maximum probability of a difference being detected by chance [10], given the observed data.

The statistical analyses performed are parametric and make use of the General Linear Model. The GLM is a statistical tool that allows the detection of regions where the GM concentration is significantly related to the effects under study, controlling for the effect of covariates, namely age, gender, disease status, among others [5]. The standard model for an across-subjects regression analysis is:

$$y_j = \boldsymbol{\beta}_j \mathbf{X} + \boldsymbol{\varepsilon}_j \quad \textbf{(2-4)}$$

where y_j is the observed value for the j^{th} subject; $\boldsymbol{\beta}_j$ is a vector of regressor variables for the j^{th} subject; $\mathbf{X}$ is a vector of parameters that varies for each voxel; $\boldsymbol{\varepsilon}_j$ is an error term. The goal is to find the best set of parameters given by $\mathbf{X}$ that best fits the model, minimizing the error [15]. In order to the statistical analysis to be valid, the residuals of the model, described as the error term, have to be normally distributed [6].

The parametric statistical analysis is based on a null hypothesis that, in this case, there are no differences in grey matter volume between the groups under study. The result is a statistical parametric map showing the voxels that refute the null hypothesis, i.e., that show significant differences. These maps can be displayed in several different ways: i) color map with the scale representing the t statistics of the test; ii) 3D surface of the brain; iii) "glass brain" in which each significant voxel is showed as greyscale in an essentially transparent render (Figure 2.8) [3].

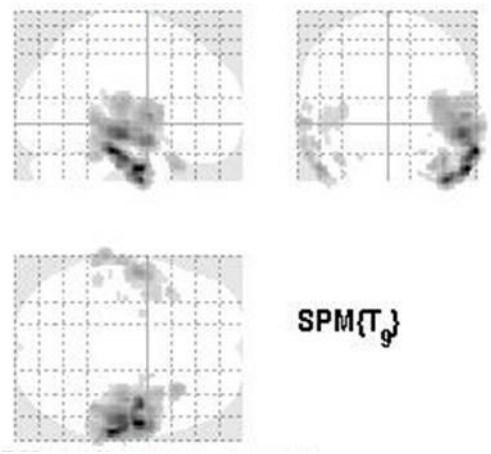

Figure 2.8 – Significant voxels shown as greyscale on a "Glass brain" display. Sagittal, coronal and axial views are shown.

As the statistical tests are performed along a large number of voxels, correction for multiple comparisons is needed in order to avoid the occurrence of false positives. The most used method is "family-wise error" (FWE) correction that controls the probability of any false positive along the whole brain.

Chapter 3

3 SMOOTHING

3.1 Basics

Prior to the statistical analysis, smoothing is performed on the segmented images. The intensity values of the segments do not follow a normal distribution, thus it is important to smooth the data in order to ensure its Gaussianization, so that the subsequent parametric statistical analysis can be performed on these data. In general, this is done by convolving the GM images with a 3D isotropic Gaussian kernel [5], characterized by its FWHM. The most frequently used kernels have an FWHM of 4, 8 and 12mm.

According to the matched filter theorem, the optimal smoothing kernel size should be related to the differences being detected [16], thus the kernel must be chosen accordingly to the study, as well as to the resolution of the acquired scans. As it is based on an arithmetic mean, by the Central Limit Theorem, smoothing renders the data more normally distributed. Hence, the validity of the posterior statistical parametric tests will be, by definition, increased.

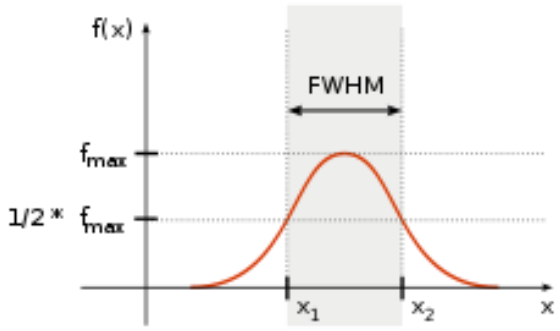

Figure 3.1 – Representation of the FWHM of a Gaussian kernel.

In addition to normality issues, the smoothing step also helps to compensate the inexact nature of the spatial normalization of the images, while also increasing the SNR. Lastly, smoothing could also help to reduce the number of statistical

comparisons, thus making the correction for multiple comparisons less severe [17].

The convolution that characterizes the smoothing step is given by Equation (3-1), where **Is** is the smoothed image, **I** is the original image and $\boldsymbol{x}$ and $\boldsymbol{\tau}$ are coordinates.

$$\mathbf{Is}(\mathbf{x}) = \int \mathbf{I}(\boldsymbol{\tau})\mathbf{G}(\mathbf{x}-\boldsymbol{\tau})d\boldsymbol{\tau} \qquad \textbf{(3-1)}$$

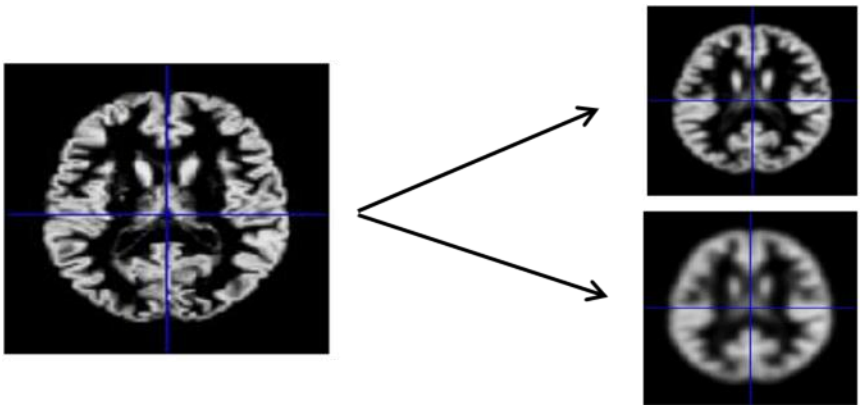

Figure 3.2 – Axial Section of a GM segment image (left); the correspondent smoothed images are shown on the right with a kernel with a FWHM of 4mm (top right) and with a FWHM of 8mm (bottom right).

As seen in Figure 3.2, the convolution of the segmented image with a Gaussian kernel results in a blurred image, compromising the anatomical definition of the smoothed image. The loss in anatomical definition is related to the size of the kernel, i.e., a smoothed image obtained with a convolution kernel with high FWHM will also have low resolution. This leads to a decrease in the ability of VBM to accurately locate changes in brain by an amount that can be approximated by the FWHM of the kernel [3]. Thereby, it is important to explore alternative ways to smooth the images, avoiding the convolution as represented in Equation (3-5).

The aim of this work is to develop methods capable of rendering the data normally distributed, without interfering with the anatomical definition, thus preserving the validity of the statistical analyses. Two alternatives were explored: i)

Gaussianization of the histogram of the images; ii) Gaussian deformation of the image coordinates.

3.2 Histogram Gaussianization

A histogram of an image is a graphical representation of the intensity distribution of that image, indicating the number of data points that lie within a range of values, called a class or a bin [18]. Hence, if the histogram is normalized, the intensities will also have a normal distribution, by definition. In theory, this normalization can be done by "equalizing" the histogram, or by using the logit transform.

3.2.1 Histogram Equalization

The histogram equalization is an image processing tool consisting in the adjustment of the contrast through the image histogram, i.e., it distributes the image intensities more uniformly along the histogram. This process approximates the histogram of the original image to a uniform histogram, computing its cumulative histogram and using it as a density function [19].

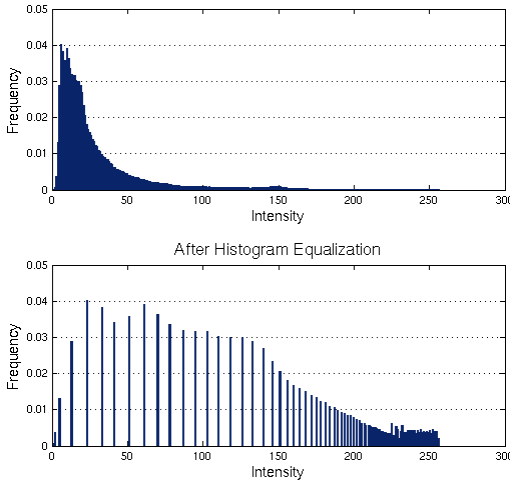

Figure 3.3 – Histogram equalization. On the top image is the histogram; on the bottom image is the correspondent equalized histogram.

Let the variable r represent the grey levels of an image, normalized to the interval [0,1]. For any r satisfying the aforementioned conditions, consider a transformation T in the form of:

$$s = T(r) \qquad 0 \le r \le 1 \qquad \textbf{(3-2)}$$

This transformation produces a new value of level for each pixel *r* in the original image. The transformation function *T(r)* has to satisfy the following conditions:

(a) *T(r)* is single-valued in the interval $0 \le r \le 1$: guarantees that the inverse transformation is possible;

(b) *T(r)* is monotonically increasing in the interval $0 \le r \le 1$: preserves the ascending order of black to white in the output image;

(c) $0 \le T(r) \le 1$ for $0 \le r \le 1$: guarantees that the grey levels of the output image are in the same range as those of the input image.

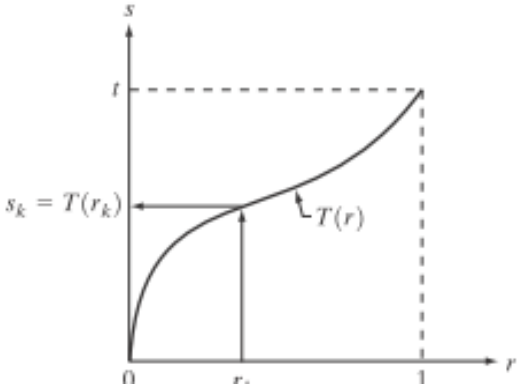

Figure 3.4 – Grey level transformation function.

The inverse transformation of *s* into *r* is given by:

$$r = T^{-1}(s) \qquad 0 \le r \le 1 \qquad \textbf{(3-3)}$$

A way to describe the grey levels of an image is with the use of a probability density function (PDF). Let $p_r(r)$ and $p_s(s)$ be the PDF's of the variables *r* and *s*, respectively. If $p_r(r)$ e $T(r)$ are known and $T^{-1}(s)$ satisfies the conditions (a) and (b) above, the PDF of *s* can be computed from the PDF of the grey levels of the input image and from the transformation chosen function. A transformation function widely used in image processing is:

$$s = T(r) = \int_0^r p_r(\omega)\, d\omega \qquad \textbf{(3-4)}$$

where ω is a dummy variable of integration. The integral of the equation can be seen as cumulative distribution function (CDF) of variable r.

With discrete values, PDF's and integrals turn into probabilities and summations, respectively. The probability of occurrence of a grey level r_k in an image is:

$$p_r(r_k) = \frac{n_k}{n} \qquad k = 0,1,2,\ldots, L-1 \tag{3-5}$$

where n is the total number of pixels in the image, n_k is the number of pixels with level r_k and L is the total number of possible levels. The discrete version of the transformation function is:

$$s_k = T(r_k) = \sum_{j=0}^{k} p_r(r_j) = \sum_{j=0}^{k} \frac{n_j}{n} \qquad k = 0,1,2,\ldots, L-1 \tag{3-6}$$

Thus, the final image is obtained by mapping each pixel with level r_k in the original image into the correspondent pixel with level s_k in the output image, using Equation (3-6) [19].

3.2.2 Logit Transform

The data can also be transformed by using the logit transformation. The logit transformation of a probability value p is given by [5]:

$$logit(p) = log\left(\frac{p}{1-p}\right) \tag{3-7}$$

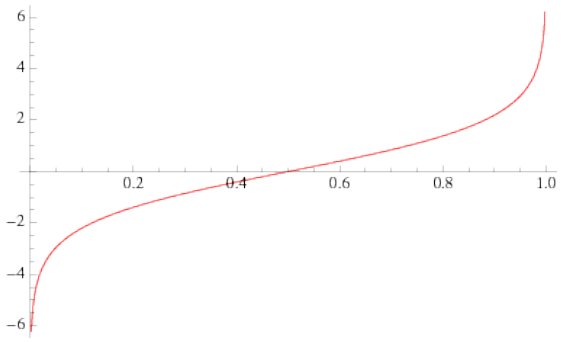

Figure 3.5 – Logit transform.

Applied to the image intensities (probabilities), ranging from 0 to 1, logit transformation maps these values to the entire real line, spreading them evenly along its histogram: negative values of logit represent probabilities below half of the range and positive values the upper half.

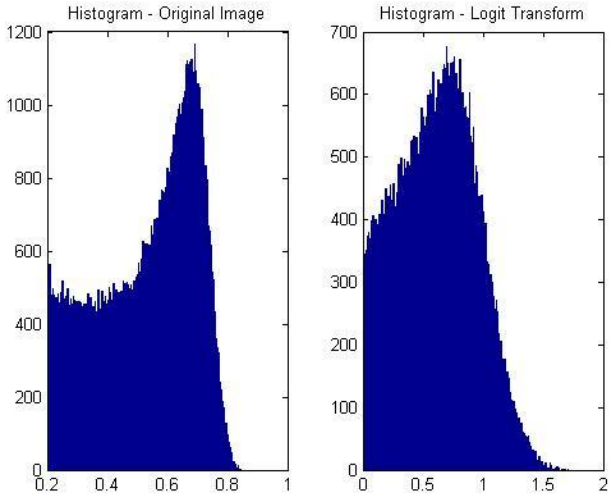

Figure 3.6 – representation of the histogram of a modulated image: before the logit transform (left) and after the logit transform (right).

As it can be seen in Figure 3.6, the histogram of the image after applying the logit transformation has a somewhat more normal distribution, nearer to a Gaussian curve.

3.3 Gaussian Deformation

Another alternative approach to the standard smoothing could be to perform the smoothing with kernel registration, i.e. create a force field around the image with vectors with arbitrary (Gaussian) amplitude and direction. In this hypothesis, the segments suffer slight changes that are strictly controlled, minimally preserving the anatomical definition and avoiding the strong deformation caused by convolution. Therefore, instead of blurring the image, it is only being changed by minor anatomical alterations so that, in the end, each coordinate could have a Gaussian distribution resultant from a controlled (Gaussian) anatomical variation.

It is not immediately clear that a Gaussian change in the anatomy of the segment could reflect in the Gaussianization of the intensity of the image. This hypothesis is sensible though, as each coordinate will suffer a Gaussian shift and, as a result, any coordinate in the resulting deformed set of images will have contributions from a random set of neighboring locations. Coupled with the interpolation in the application of the deformations fields, each coordinate of the image will represent a local average of intensities – in essence, the same as the Gaussian "blurring" explained above.

The alteration of the shape of the segments is made by the vector field with random direction and amplitude, so that a new coordinate (x',y',z') is obtained by:

$$(x', y', z') = (x, y, z) + \alpha \cdot randn(x, y, z) \quad \textbf{(3-8)}$$

The variable α is a scale factor representing the maximum norm of the deformation vectors.

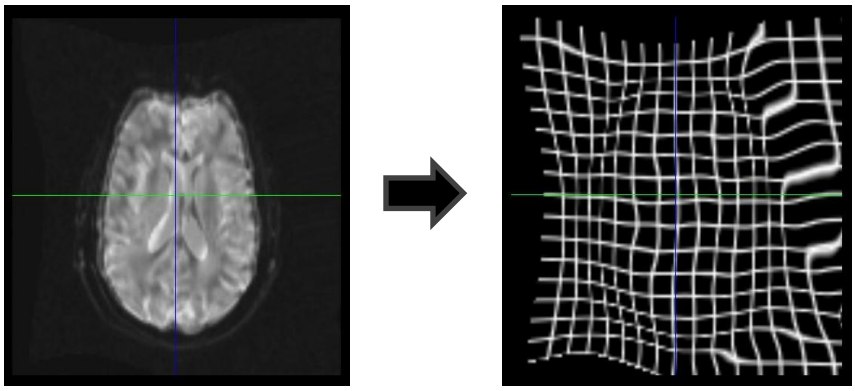

Figure 3.7 – Schematic of the deformation process performed by the vector field with random direction and amplitude (2D).

When the segmented image is registered in the new grid, the final coordinates may not correspond to the locations in the original grid. Thus, an interpolation of the values of the voxels belonging to the existing grid is performed in order to calculate the values of the voxels placed in arbitrary positions in the new grid. In this new transformed grid, the coordinates will have new intensities values I, obtained by linear interpolation. Assuming a simple one dimensional example, the

intensity of the arbitrary position **x'** is calculated by a distance weighted average of the intensity of its grid neighbors:

$$\mathbf{x}' = \omega\mathbf{x}_1 + (1-\omega)\mathbf{x}_2 \Rightarrow I(\mathbf{x}') = \omega I(\mathbf{x}_1) + (1-\omega) I(\mathbf{x}_2) \quad \textbf{(3-9)}$$

where $\mathbf{x}_1$ and $\mathbf{x}_2$ are the grid neighbors of **x'**, ω is the normalized Euclidean distance between **x'** and $\mathbf{x}_1$ and $I(\mathbf{x})$ is the image intensity at location **x**. In 3D, this interpolation is called trilinear interpolation and requires the use of Equation (3-9) in all three dimensions, leading to the concatenation of 3 linear interpolations [10].

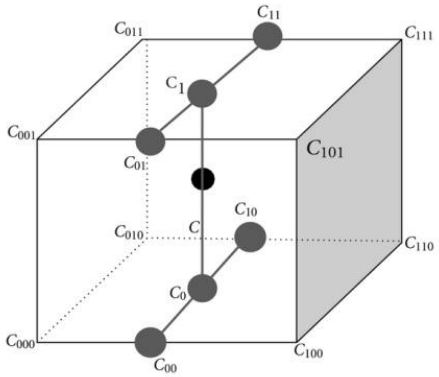

Figure 3.8 – Schematic of how a trilinear interpolation calculates the value at the arbitrary location c (black dot). The vertices represent the known values (grid) and the grey dots represent interpolated values.

This method of Gaussianization was applied to the registered and modulated segments of GM using two different approaches: i) making use of the Central Limit Theorem; ii) using an iterative Gaussian deformation of the images.

3.3.1 Central Limit Theorem

As seen above, it is hypothesized that the Gaussianization of the GM segmented images can be achieved through controlled, low amplitude anatomical deformations of the segments. One way to implement this method is to make use of the Central Limit Theorem (CLT): given a sufficient large number of iterates of independent variables with a well-defined variance, the mean of all iterates will follow an approximate normal distribution pattern [20]. Thus, the original segment

can be formed n times, using a single application of a random (Gaussian) vector field each time, and then the average of all anatomical changes is computed (Figure 3.9): by the Central Limit Theorem, the distribution should be more Gaussian. To evaluate this process, a number of iterations from 5 to 100 was considered, with increments of 5; the scale factor α was assumed to be 1 or 3.

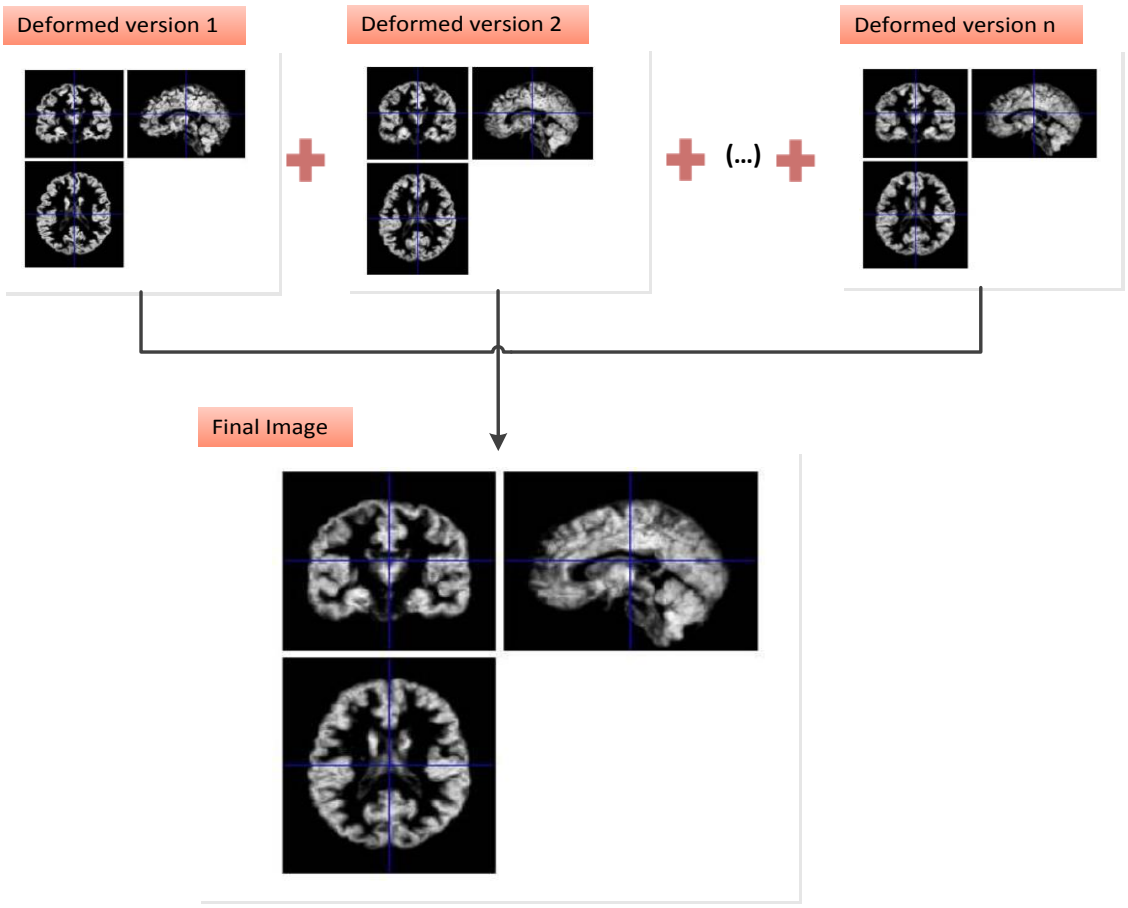

Figure 3.9 – Schematic of the smoothing method with Gaussian deformation, with the CLT, using n iterations and $\alpha = 1$.

As seen in Figure 3.9, at the end of each iteration, a new image is produced through the interpolation of the voxels of the original image into the voxels of the new grid, formed by the deformation vectors. When all iterations are completed, an average of all the images is performed and a final smoothed image is achieved.

3.3.2 Iterative Gaussian Deformation

The normalization of the segments can also be achieved through a process of iterative deformation. This method as some similarities with the one explained in the previous Section as the coordinates are also deformed through a Gaussian vector field. In the first method, an average of all the anatomical changes is computed and, by the central limit theorem, the spatial distribution will be more Gaussian. In this second method, each coordinate is also being deformed and interpolated to its new arbitrary positions, but this process is repeated with the same image in an iterative progressive way (Figure 3.10). To evaluate this process, a number of iterations from 1 to 10 was considered; the scale factor α was assumed to be 1 or 3.

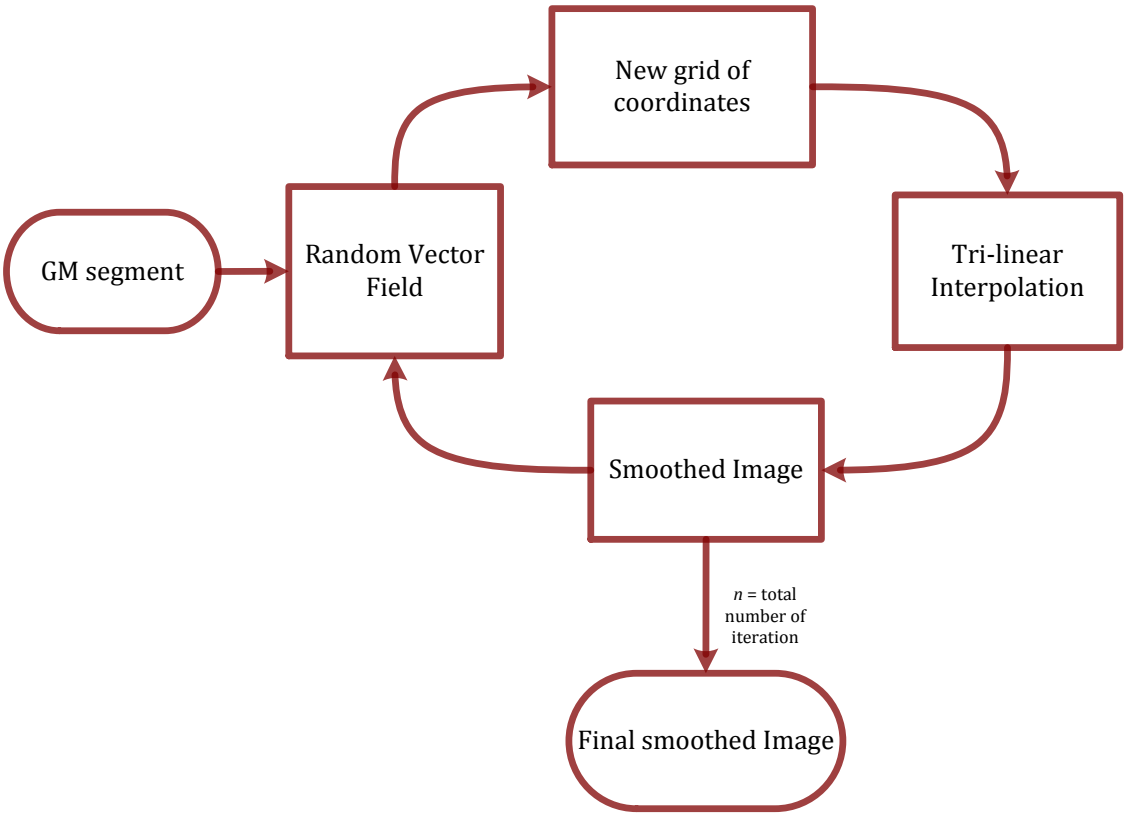

Figure 3.10 – Flowchart of the Iterative Gaussian deformation process.

As explained in Section 3.3, a random vector field is applied to the segments, changing its coordinates and forming a new grid: the final, smoothed image is obtained through tri-linear interpolation on top of the previous version of the

deformation image. At the end of each iterate, the resulting altered image is resubmitted to the process until the whole process is completed.

3.4 Assessment of normality

As seen in Section 2.2.5, VBM uses parametric statistical tests and the GLM in order to produce the statistical parametric maps of regions of interest in brain. The residuals of the GLM must follow a Gaussian distribution for it to be valid though. Prior to smoothing, the segments usually have a highly non-normal distribution and, consequently, the error distribution about any group mean will have a similar non-normal distribution [6].

The spatial smoothing as done with the standard method usually ensures the normality of the data. However, even then there can be some circumstances that may lead do deviations from normality, invalidating the statistical tests. One example concerns the designs used: in unbalanced designs (different number of subjects in both groups to be compared) usually the differences lead to non-normal distributions and the consequent analysis will not conform to parametric assumptions [6]. Therefore, is of extreme relevance evaluate the normality of the data. In this thesis in particular, this statement is even truer as the alternative Gaussianization methods need to be assessed quantitatively.

Statistics cannot prove that the data is normally distributed, but it is possible to quantify the degree of non-normality [5]. In this work, a QQ plot analysis was performed, followed by an ROI analysis to assess the normality of the data.

3.4.1 QQ plot

A QQ plot is a plot of the quantiles of the sample distribution vs the expected quantiles in case of a given (in this case, normal) distribution. When the plots lie very closely to a straight line, the normality assumption is acceptable. Deviations from this line can be computed through its correlation coefficient r_Q.

Considerer x_1, x_2, …, x_n the n observations of the model residuals and the q_1, q_2, …, q_n their distribution quantiles. The steps to compute a QQ plot are:

1. Sort the residuals in ascending order (x_1, x_2, …, x_n) and get their correspondent probability values (1-1/2)/n, (2-1/2)/n, …, (n-1/2)/n;
2. Estimate the standard normal quantiles q_1, q_2, …, q_n (obtained from a lookup table);
3. Plot the observation pairs (q_1,x_1), (q_2,x_2), …, (q_n,x_n) and examine the "straightness" of the output.

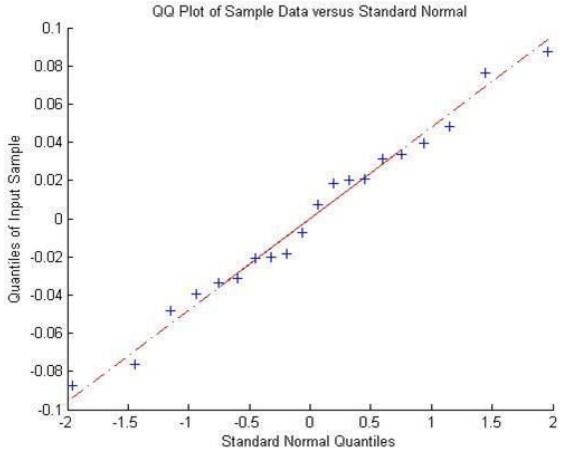

Figure 3.11 – QQ plot for the residuals of a GLM applied to a set of 20 subjects.

If the correlation coefficient (Equation (3-10)), used to test significant deviations from a straight line, falls below a certain value, given a sample size, non-normality can be inferred [6]. Hence, it is possible to compute the proportion of elements whose coefficient is smaller than the threshold value, i.e. it is possible to infer about the degree of non-normality. According to the literature, given the sample size used (n=20), the correlation coefficient threshold is 0.92 [15].

$$r_Q = \frac{\sum_{j=1}^{n}(x(j)-\bar{x})(q(j)-\bar{q})}{\sqrt{\sum_{j=1}^{n}(x(j)-\bar{x})^2}\sqrt{\sum_{j=1}^{n}(q(j)-\bar{q})^2}} \qquad \textbf{(3-10)}$$

As the GLM is applied on a voxel-by-voxel basis (massive univariate approach in VBM as seen in Section 2.2), this assessment of residuals is also performed on each coordinate. As such, it is possible to evaluate the proportion of voxels that fall

below this minimum threshold out of the entire sample of voxels under analysis: this proportion is a measure of the non-normality of the data.

3.4.2 ROI Analysis

The method described in the previous Section gives information about the normality process across the whole brain. Nonetheless, it would be interesting to have an analysis by regions of interest to evaluate the regional impact on the normality of the data. This could be achieved by performing a ROI analysis on the proportions described above.

For the purpose of this thesis, this analysis was used to study the non-normality behavior of five different regions of the brain: frontal, parietal, occipital and temporal lobes and cerebellum.

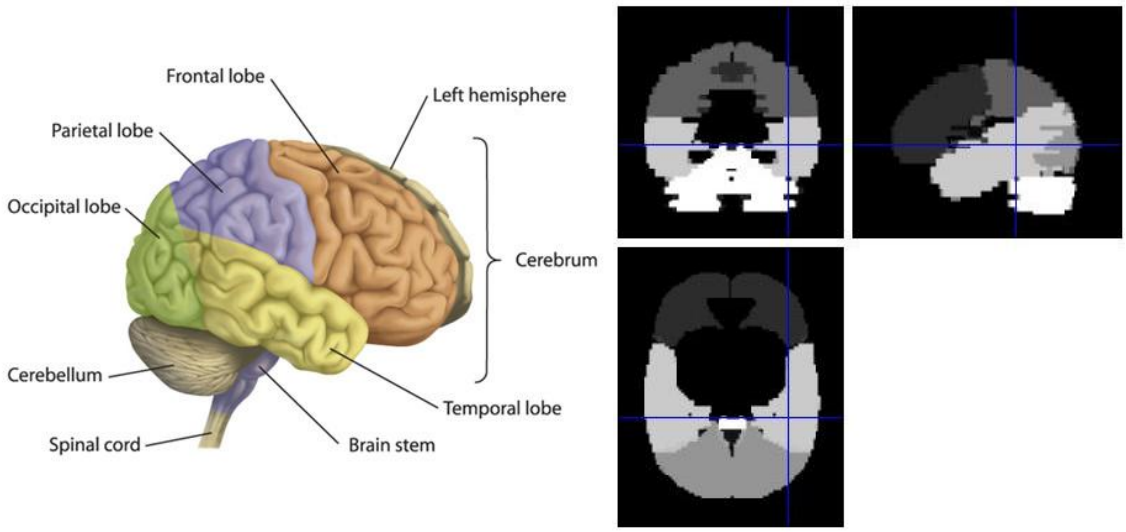

Figure 3.12 - Representation of the right hemisphere of the brain divided into its main regions (left); sagittal, coronal and axial views of the brain mask of frontal, parietal, occipital and temporal lobes and cerebellum used in the ROI analyses (right).

Applying the previously described method to each of the regions, one can compute the number of voxels that violates the normality hypothesis within each region and, consequently, the regional degree of non-normality.

Chapter 4

4 RESULTS

4.1 Methods

4.1.1 Subjects and Imaging

Twenty healthy controls were scanned coronally on a 1.5-T GE Signa MRI scanner (GE Medical Systems, Milwaukee, WI, USA) using a T1-weighted 3-D IR-FSPGR sequence (echo time: 4.2 ms, inversion time: 650 ms and flip angle: 20°) with voxel size 0.86×0.86×1.5 mm.

Of these, a random subset of ten scans was re-sampled to 256×256×256 (1-mm isotropic) using sinc interpolation. The GUI tkmedit function in FreeSurfer v.3.04 was used to manually mask GM voxels in the temporal lobe and insula of all subjects; the removal being more intense on the right side Figure 4.1. This served to create a ground truth simulated lesion or atrophy profile so that the visual assessment of results could be more robust.

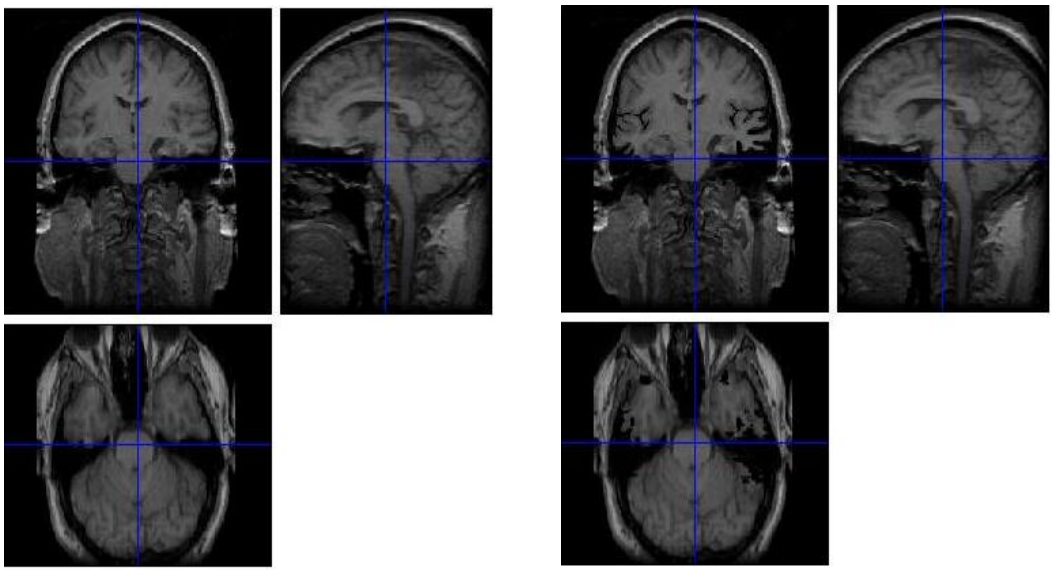

Figure 4.1 – Coronal, sagital and axial views of the brain of a control subject (left) and the correspondent edited subject (right).

4.1.2 Standard VBM analyses

To visually assess the impact of the methods described in this thesis, the subset of ten edited scans (with their original counterparts) mentioned in the previous Section were subjected to a standard VBM analyses, performed in SPM8 (http://www.fil.ion.ucl.ac.uk/spm/). Firstly, all the images were registered and segmented into grey matter using the standard unified segmentation method [14]. The segmentation step was also performed with a modulation step. These registered, segmented and modulated images were used to implement and evaluate the developed methods, described in Section 3.

The GM segments were smoothed with the standard method by convolving the grey matter segments with Gaussian kernels with FWHM of 4mm and 8mm. Additionally, VBMs were also performed without any smoothing and with a selection of "best performers" (defined below) from the methods described in Chapter 3 and developed in the context of this thesis.

Finally, the parametric statistical analysis was applied to the resulting images, choosing a paired t-test where the aforementioned group of 10 control subjects was compared to their edited counterparts. A relative threshold masking of 0.2 was used, i.e. only coordinates where over 20% of voxels included grey matter were included in the analysis. The t-contrast used in the model was [1 -1] (control vs edited) and the statistical threshold used was 0.05, FWE corrected. The extent threshold (minimum number of voxels included in a cluster of significance) was set at zero to get the full perspective of the impact of the smoothing method on the VBM.

4.1.3 Alternative smoothing

As referred in Sections 3.2 and 3.3, two main methods were developed as alternative ways to smooth the data: Histogram Gaussianization and Gaussian Deformation. Both techniques were applied to the segmented images mentioned in the previous Section. All the methods were implemented and assessed using Matlab 2011b (The Mathworks Inc, Natick, MA).

4.1.3.1 Histogram Gaussianization

The Histogram Gaussianization method consisted in normalizing the histograms of the images, as explained in Section 3.2. To do that, two techniques were used: i) the histogram equalization was performed with *histeq* Matlab function; and ii) the Logit Transform was performed with *logit* Matlab function.

4.1.3.2 Gaussian Deformation

As seen in Section 3.3, the grey matter segments images can also be smoothed through the application of a force field with vectors with arbitrary amplitude and direction. This results in a new grid of coordinates in which, it is hypothesized, each coordinate has a Gaussian distribution.

The random vectors are computed using the function *randn*. The new grid of coordinates was calculated using the function *meshgrid*:

$$[X,Y,Z] = meshgrid(1:ax,1:ay,1:az) \quad \textbf{(4-1)}$$

where *X*, *Y* and *Z* are 3D coordinate arrays and *(1:ax)*, *(1:ay)* and *(1:az)* are coordinate vectors with lengths corresponding to the dimensions of the original images. This mesh was "jittered" using Gaussian vectors and the intensity of the voxels in the new coordinates was calculated by resorting to the *interp3* function, using trilinear interpolation.

This method was applied in two different ways and a different number of iterations was used in both approaches, as explained in Section 3.3.

4.1.4 Normality assessment

4.1.4.1 GLM

To assess the normality of the data after smoothing, the General Linear Model was applied to the images. As seen in Section 2.2.5, the GLM is used in VBM to detect significant differences in the GM concentration between two groups being

compared, controlling for covariates. The model can also be used for multilinear regression purposes, which was the case for this assessment:

$$\mathbf{Y} = \boldsymbol{\beta}_1 age + \boldsymbol{\beta}_2 gender + \boldsymbol{\beta}_3 TGMV + \boldsymbol{\varepsilon} \quad \textbf{(4-2)}$$

where **Y** is a matrix containing the intensity values of the voxels of grey matter segment, $\boldsymbol{\beta}_1$, $\boldsymbol{\beta}_2$ and $\boldsymbol{\beta}_3$ are the regressors that explain the relation between the independent variables and **Y**, while age, gender and total grey matter volume (TGMV) are the independent variables whose values compose the design matrix of the model, and $\boldsymbol{\varepsilon}$ is the vector of residuals. This is a fairly arbitrary model, but one that can be used for this purpose as it is known that these independent variables affect grey matter volume [10].

In order to have statistical significance, the model was applied 12 times, each time to a set of 10 randomly selected scans from the total of 20 scans mentioned above. This was done for every smoothing method in order to get a pool of residual values for each.

The last part of the model, $\boldsymbol{\varepsilon}$, is a random variable that contains the variability of **Y** that the model is unable to explain. For the model to be valid is necessary to ensure that this variable assumes a Gaussian distribution: it is therefore essential to assess the normality of its distribution.

4.1.4.2 QQ plot and Correlation Coefficient

To assess the normality of the residuals, a QQ plot analysis was performed. As seen in Section 3.4.1, by computing the correlation coefficient r_Q of the QQ plot, one can obtain the proportion of voxels with an r_Q below a certain threshold and, thus, infer about the degree of non-normality of the data. The correlation coefficient was computed with Equation (3-10). For each time the model was applied, the number of voxels with r_Q<0.92 was calculated and the proportion (out of the total) of voxels that violated the hypothesis of normality as assessed by this threshold was obtained and the respective mean was represented in bar graphs.

This correlation coefficient was calculated with the images obtained with the standard VBM, with kernels of 4mm and 8mm and with no smoothing, making a

total of three (mean) proportion values. These results were compared between each other in order to locate significant differences between them. All statistical analyses were performed with SPSS (IBM Corp. Released 2011. IBM SPSS Statistics for Windows, Version 20.0. Armonk, NY: IBM Corp.). The non-parametric statistical test of Kruskal-Wallis was used due to the low number of elements in each sample (n=12), with Mann Whitney post-hoc tests with Bonferroni correction. The resulting p-values of the tests were used to evaluate the significance of the differences between the methods.

The same process was repeated for the developed methods. In case of the Gaussian deformation, the proportion of data points violating the normality hypothesis was obtained for each of the iterations and scale factor α used. For each method, the results were compared with the ones obtained with the standard smoothing, using the same statistical tests mentioned before.

4.1.4.3 ROI Analysis

Subsequent to the QQ plot analysis, a ROI analysis was performed, as explained in Section 3.4.2. The aim of the ROI analysis is to study the normality within regions of the brain, namely frontal, parietal, occipital and temporal lobes and cerebellum, and see if there is a spatial pattern of non-normality.

Firstly, a mask of the whole brain showing the voxels with a non-normal distribution was computed and it was superimposed to a standard brain in MNI space, providing information about the normality of the data across the whole brain. This was achieved by coding an in-house function in Matlab.

Secondly, the division of the brain into its regions was performed using WFU_PickAtlas (Version 3.0.4.). Then, the number of voxels with a non-normal distribution in each region was computed and the correspondent proportion (out of the total under actual analysis) of non-normal data points in each region was obtained.

4.2 Standard Smoothing

The results for the standard smoothing and no smoothing VBM are shown below: the proportion of data points that significantly violate the assumption of normality can be seen in Figure 4.2, and the respective differences in Table 4.1.

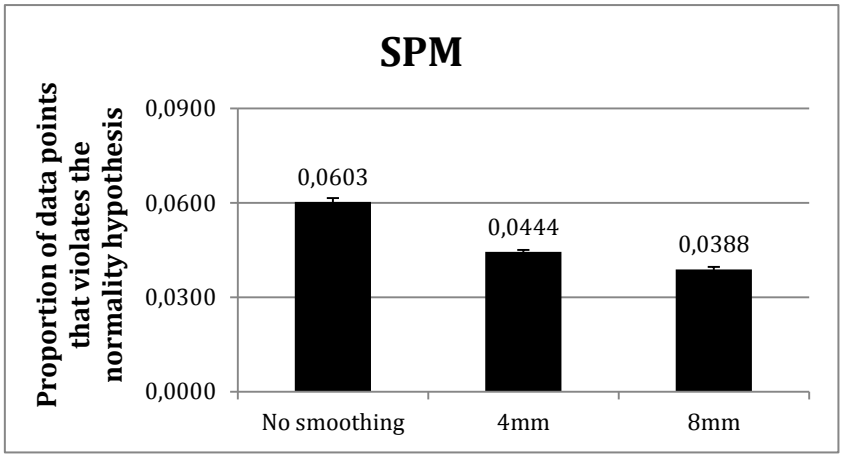

Figure 4.2 – Proportion of data points significantly violating the assumptions of normality with no smoothing, with 4mm and 8mm smoothing. The bars represent one standard error.

Table 4.1 - Differences between the three groups (no smoothing, 4mm and 8mm), given by the p-value of the pairwise comparisons (post hoc with Bonferroni correction).

Kruskal – Wallis	
Sample1-Sample2	**p-value**
8mm-4mm	0,480
8mm-No smoothing	<0,001
4mm-No smoothing	<0,001

The ROI analysis was then applied to the images with no smoothing, with 4mm and 8mm smoothing: the regional distribution of non-normal voxels is represented in Figure 4.3, as well as all the voxels considered for analysis. The regional proportion of non-normal voxels was then obtained for each ROI under analysis (Figure 4.4). Finally, the VBM analysis was performed using the second group of subjects, 10 controls and the same 10 subjects manually edited, as explained in Section 4.1.1,

and the resulting SPM of the images with no smoothing, with 4mm smoothing and 8mm smoothing can be seen in Figure 4.5.

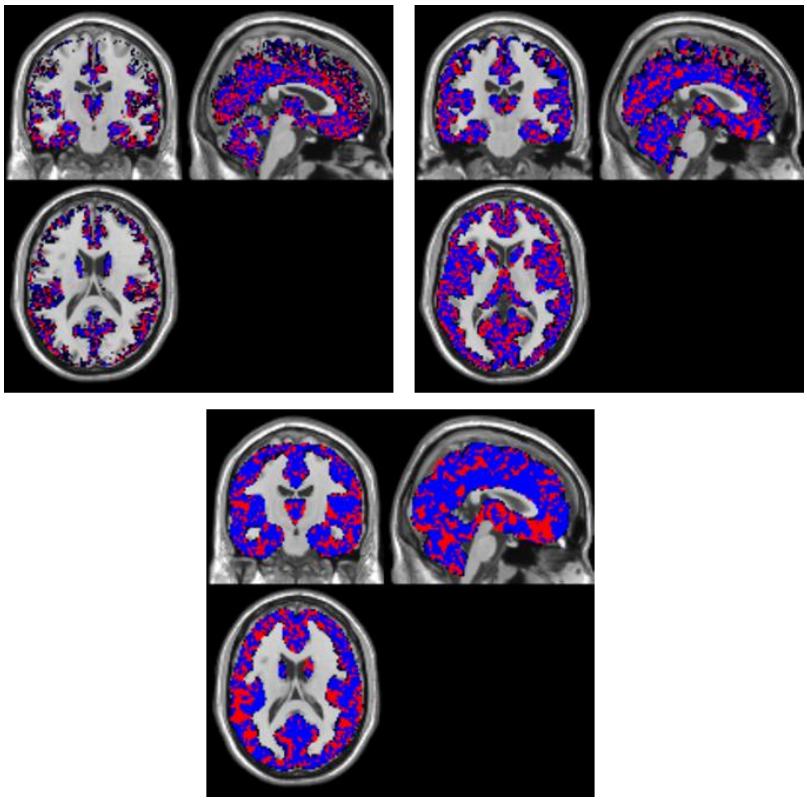

Figure 4.3 - Representation of the regional distribution of non-normal voxels (red) for the images with no smoothing (top left), 4mm smoothing (top right) and 8mm smoothing (bottom). The blue regions represent the regions that were considered in the analysis.

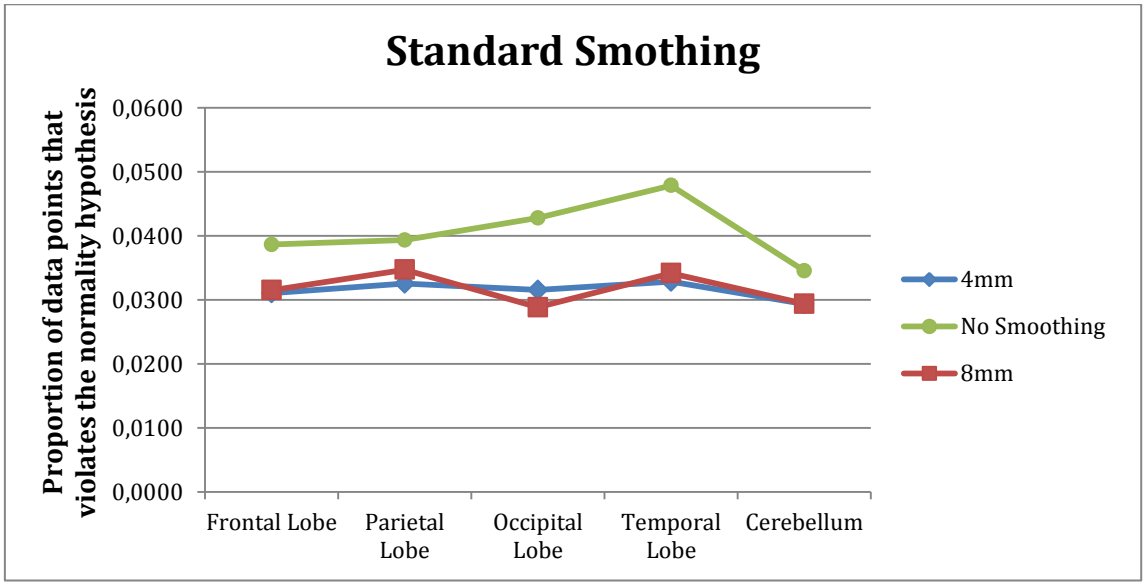

Figure 4.4 – Regional proportion of non-normal voxels for the images with no smoothing (green), 4mm (blue) and 8mm (red) smoothing.

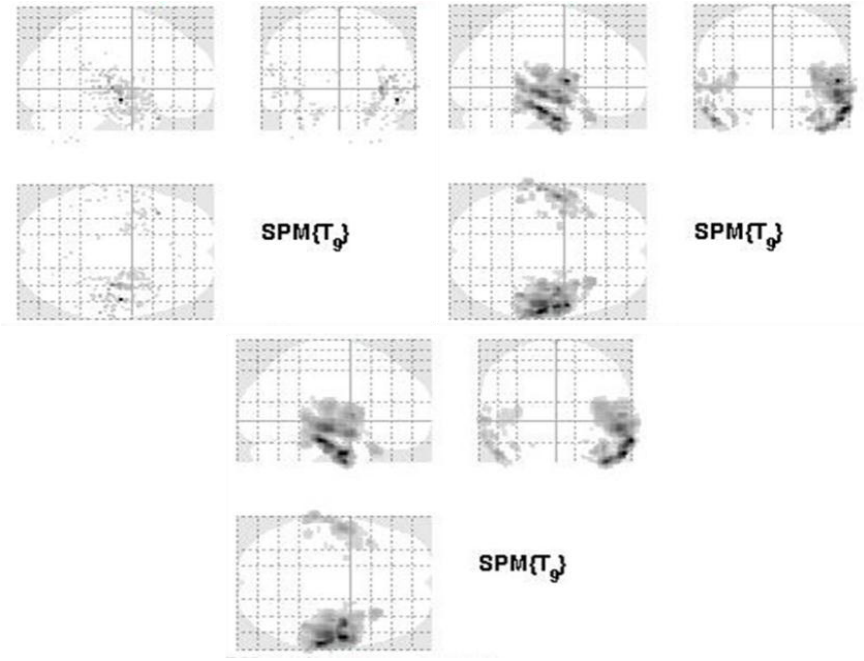

Figure 4.5 - Statistical parametric map resulting of the VBM analysis of the images with no smoothing (top left), with 4mm (top right) and 8mm (bottom) smoothing.

4.3 Histogram Gaussianization

After applying the histogram Gaussianization methods to the 20 modulated subjects, the GLM was applied as explained above and the normality of the data was assessed through the residuals of the model. The proportion of non-normal voxels and the respective differences are shown in Figure 4.6 and Table 4.2, respectively.

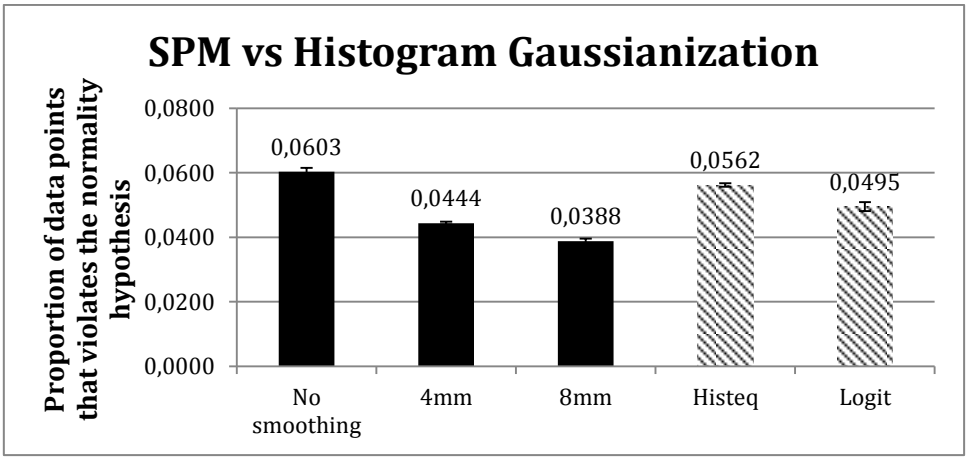

Figure 4.6 - Proportion of data points significantly violating the assumptions of normality with no smoothing, with 4mm and 8mm smoothing (bold) and with histogram equalization and logit transform (striped). The bars represent one standard error.

Table 4.2 - Differences between the groups (no smoothing, 4mm and 8mm, histogram equalization and logit transform), given by the p-value of the pairwise comparisons (post hoc with Bonferroni correction).

Kurskal-Wallis			
Sample1-Sample2	**p-value**	**Sample1-Sample2**	**p-value**
No smoothing-Histeq	1,000	4mm-Logit	1,000
No smoothing-Logit	0,444	8mm-Histeq	0,003
4mm-Histeq	0,153	8mm-Logit	0,575

The histogram equalization method does not provide a reasonable result in terms of data normalization, as it can be seen in Figure 4.6. Moreover, Table 4.2 shows that there are significant differences between this method and the smoothing with the 8mm Gaussian kernel, which is not in accordance with what is intended, since the aim is that the developed methods provide an equivalent or improved ability to normalise the data when compared to the standard smoothing. Thereby, in further analyses, namely regional distribution and proportion of non-normal voxels and VBM, only the logit method will be considered.

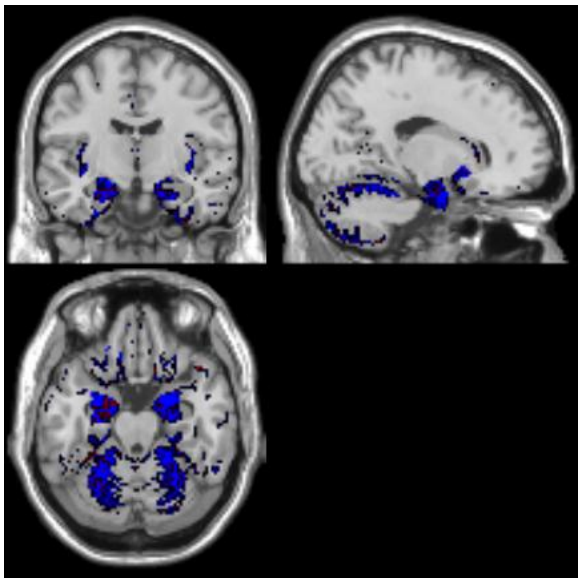

Figure 4.7 - Representation of the regional distribution of non-normal voxels (red) for the images smoothed with logit transform. The blue regions represent the regions that were considered in the analysis.

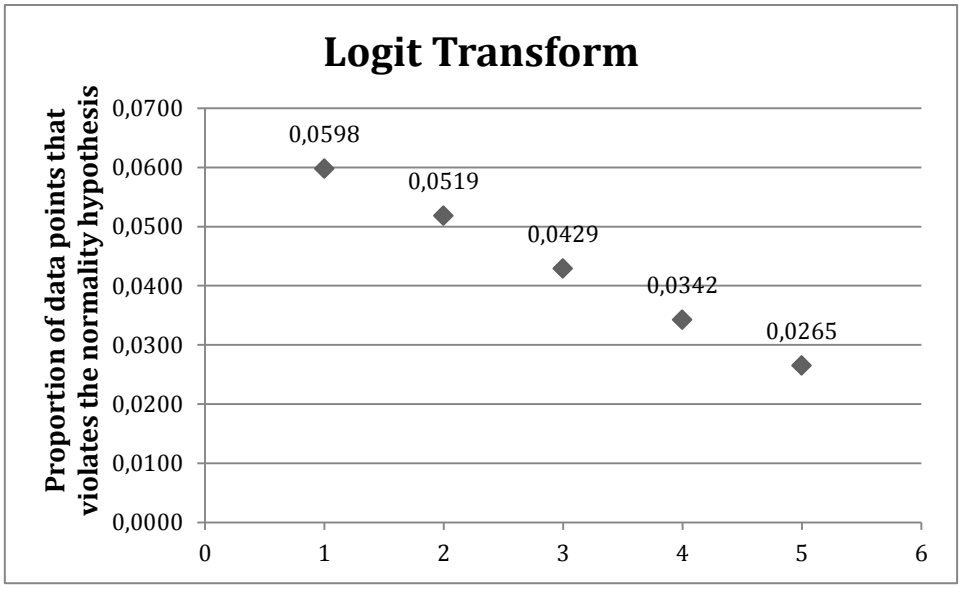

Figure 4.8 - Regional proportion of non-normal voxels for the images smoothed with the logit transform.

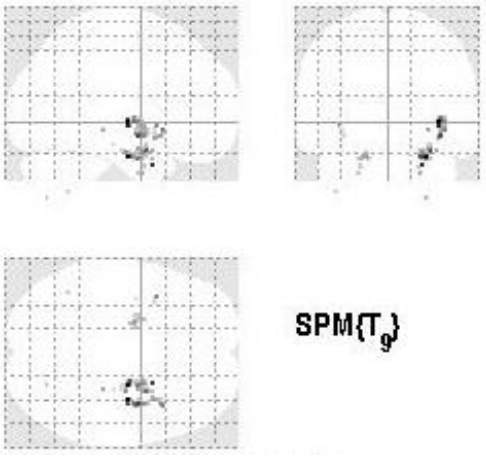

Figure 4.9 - Statistical parametric map resulting of the VBM analysis of the images smoothed with the logit transform.

4.4 Gaussian Deformation

4.4.1 Central Limit Theorem

This method was applied taking into account two variables: number of iterations n and scale factor α. The total number of iterations was initially performed for $\alpha = 1$ and only the best results were then used to test the effect of using $\alpha = 3$.

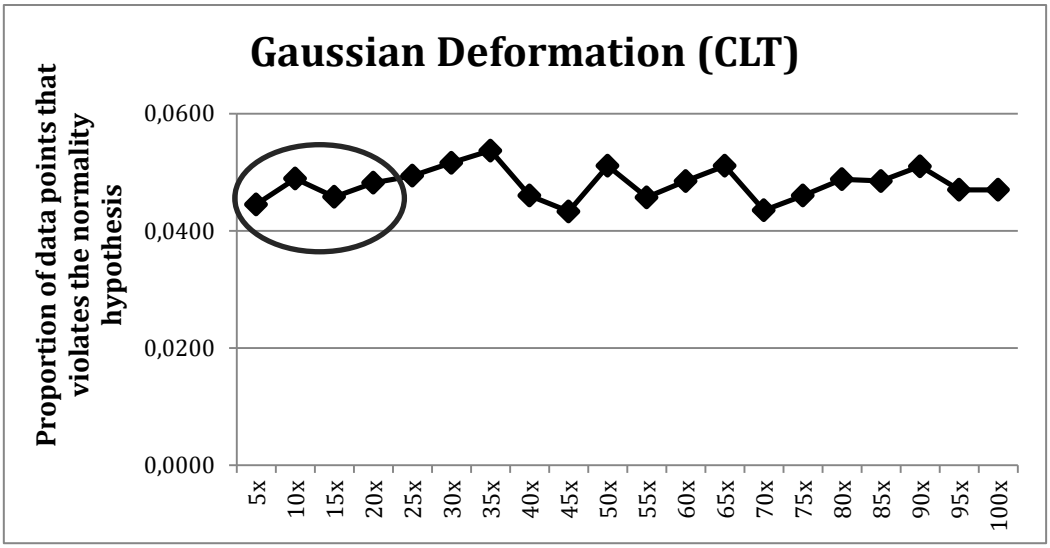

Figure 4.10 – Proportion of data points violating the assumptions of normality of the smoothed images as a function of the number of iterations used.

The first four points of the chart (marked with the circle) shown in Figure 4.10, corresponding to 5, 10, 15 and 20 iterations, were chosen to evaluate this method and, thus, further analyses were only performed using the images obtained with these criteria.

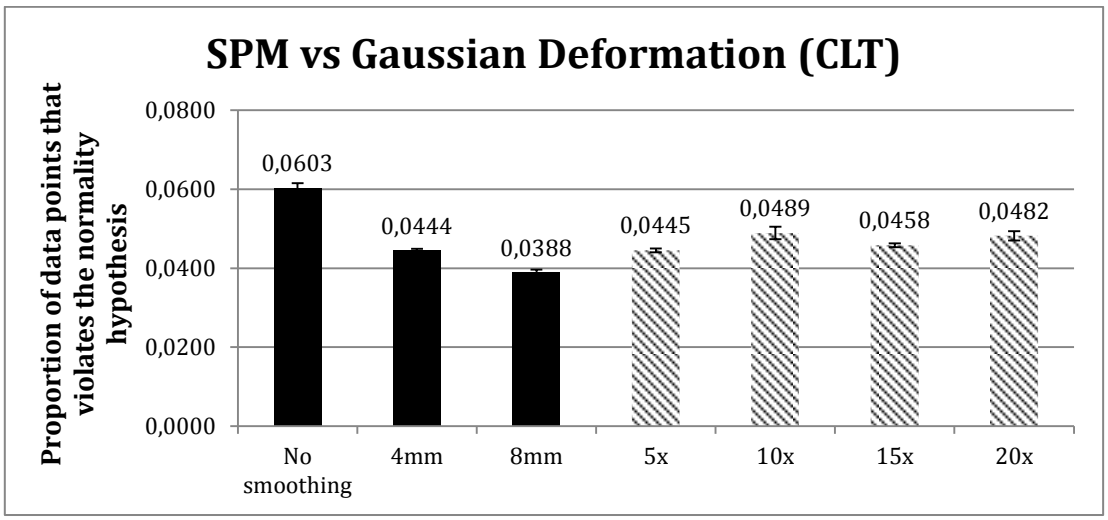

Figure 4.11 - Proportion of data points significantly violating the assumptions of normality with no smoothing, with 4mm and 8mm smoothing (bold) and with Gaussian deformation by the Central Limit Theorem, using α=1 (striped). The bars represent one standard error.

Table 4.3 - Differences between groups (no smoothing, 4mm and 8mm and Gaussian deformation for n=5, 10, 15 and 20 with α=1), given by the p-value of the pairwise comparisons (post hoc with Bonferroni correction).

Kruskal - Wallis			
Sample1 – Sample2	**p-value**	**Sample1 – Sample2**	**p-value**
No smoothing - 5x	0,024	4mm - 15x	1,000
No smoothing - 10x	0,024	4mm - 20x	1,000
No smoothing - 15x	0,060	8mm - 5x	1,000
No smoothing - 20x	0,012	8mm - 10x	0,744
4mm - 5x	1,000	8mm - 15x	0,312
4mm - 10x	1,000	8mm - 20x	0,516

The same number of iterations was used to test the effect of using α = 3.

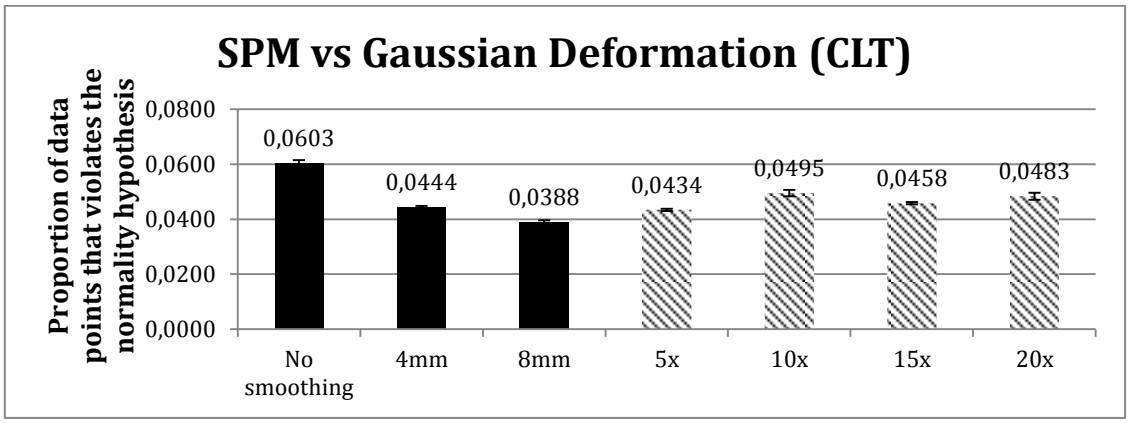

Figure 4.12 - Proportion of data points significantly violating the assumptions of normality with no smoothing, with 4mm and 8mm smoothing (bold) and with Gaussian deformation by the Central Limit Theorem, using α=3 (striped). The bars represent one standard error.

Table 4.4 - Differences between groups (no smoothing, 4mm and 8mm and Gaussian deformation for n=5, 10, 15 and 20 with α=3), given by the p-value of the pairwise comparisons (post hoc with Bonferroni correction).

Kruskal - Wallis			
Sample1 – Sample2	**p-value**	**Sample1 – Sample2**	**p-value**
No smoothing - 5x	0,012	4mm - 15x	1,000
No smoothing - 10x	0,192	4mm - 20x	1,000
No smoothing - 15x	0,192	8mm - 5x	1,000
No smoothing - 20x	0,072	8mm - 10x	0,180
4mm - 5x	1,000	8mm - 15x	0,180
4mm - 10x	1,000	8mm - 20x	0,456

According to Figure 4.11 and Figure 4.12, the best result while using the scale factor α=1 was found for a number of iterations n=5 (proportion of 0.0445), as well as using α=3 (proportion of 0.0434). Hence, the images obtained with these

specifications were used to find the results in terms of regional distribution of non-normality as well as for the VBM analysis.

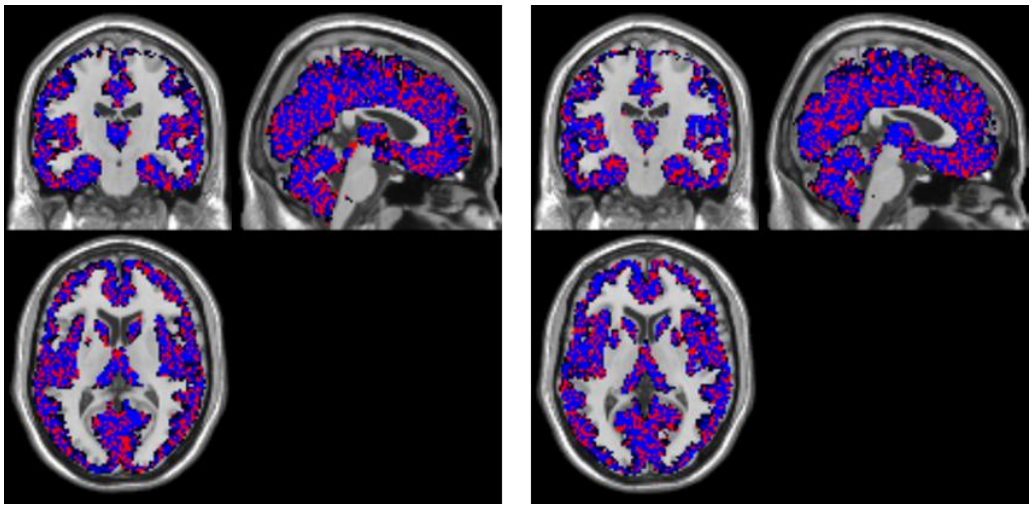

Figure 4.13 - Representation of the regional distribution of non-normal voxels (red) for the images smoothed with Gaussian deformation method (CLT), for iterations n=5 with α=1 (left) and n=5 with α=3 (right). The blue regions represent the regions that were considered in the analysis.

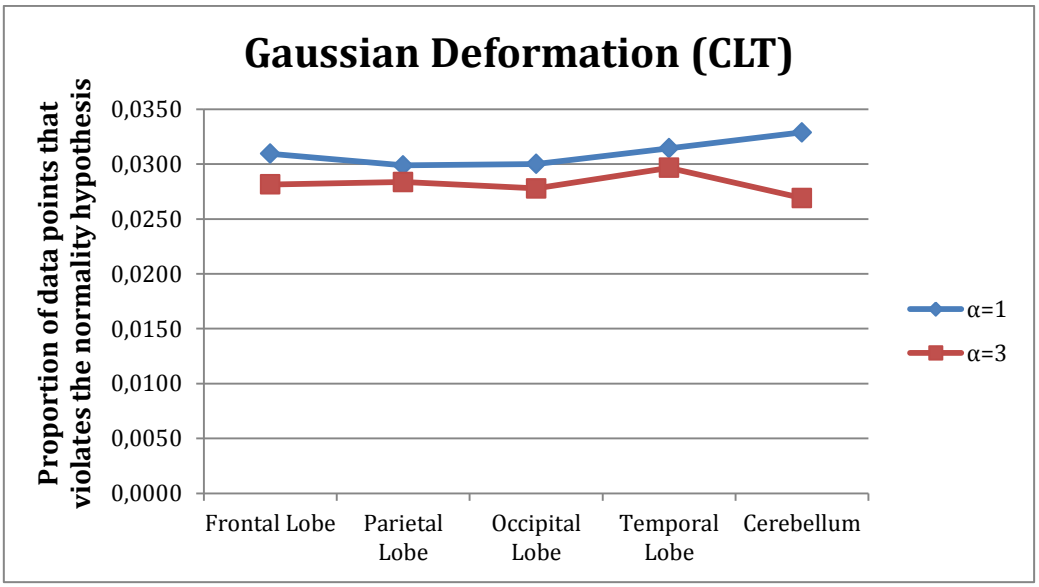

Figure 4.14 - Regional proportion of non-normal voxels for the images smoothed with Gaussian deformation method (CLT), for iterations n=5 with α=1 (blue) and n=5 with α=3 (red).

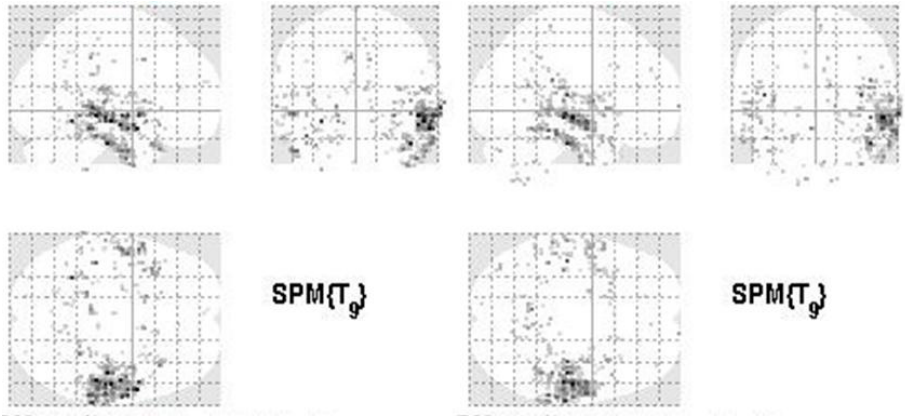

Figure 4.15 - Statistical parametric map resulting of the VBM analysis of the images smoothed with Gaussian deformation method (CLT), for iterations *n*=5 with *α*=1 (left) and *n*=5 with *α*=3 (right).

4.4.2 Iterative Gaussian Deformation

As seen in Section 4.4.1, this method was also applied while varying the number of iterations *n* and scale factor *α*. As before, the total number of iterations was performed for *α* = 1 and only the best results were used to test the effect of using *α* = 3.

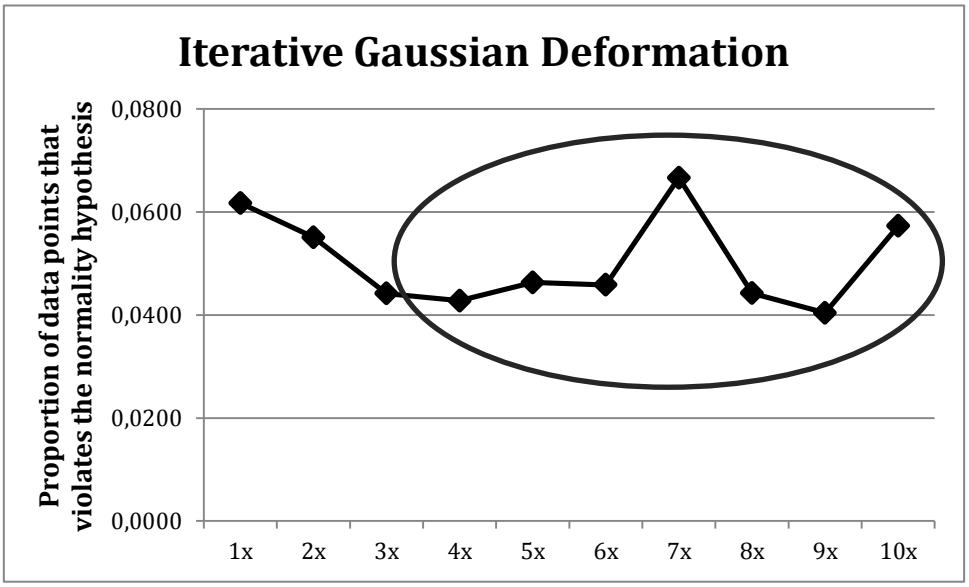

Figure 4.16 - Proportion of data points violating the assumptions of normality of the smoothed images as a function of the number of iterations used.

The points marked in the chart in Figure 4.16, corresponding to 3, 4, 5, 6, 7, 8, 9 and 10 iterations, were chosen to evaluate this method and, thus, further analyses were only performed using the images obtained with these criteria.

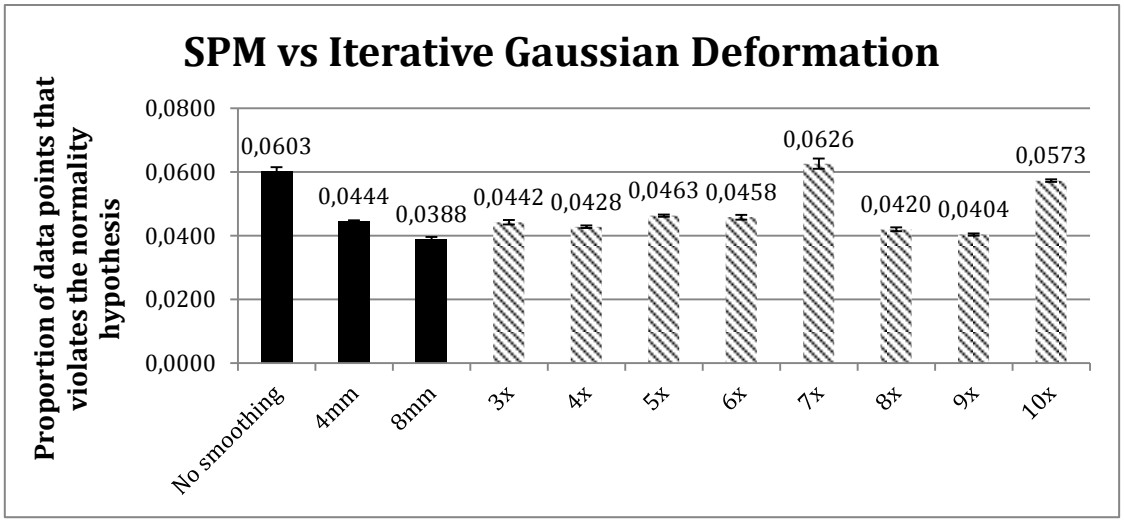

Figure 4.17 - Proportion of data points significantly violating the assumptions of normality with no smoothing, with 4mm and 8mm smoothing (bold) and with iterative Gaussian deformation, using α=1 (striped). The bars represent one standard error.

Table 4.5 - Differences between the groups (no smoothing, 4mm and 8mm and Gaussian deformation for n=3, 4, 5, 6, 7, 8, 9 and 10), given by the p-value of the pairwise comparisons (post hoc with Bonferroni correction).

Kruskal - Wallis			
Sample1 – Sample2	**p-value**	**Sample1 – Sample2**	**p-value**
No smoothing - 3x	0,024	4mm-7x	1,000
No smoothing - 4x	<0,001	4mm-8x	1,000
No smoothing - 5x	<0,001	4mm-9x	1,000
No smoothing - 6x	<0,001	4mm-10x	0,024
No smoothing - 7x	0,792	8mm-3x	1,000
No smoothing - 8x	<0,001	8mm-4x	1,000
No smoothing - 9x	<0,001	8mm-5x	0,312
No smoothing - 10x	1,000	8mm-6x	1,000
4mm-3x	1,000	8mm-7x	<0,001
4mm-4x	1,000	8mm-8x	0,996
4mm-5x	1,000	8mm-9x	1,000
4mm-6x	1,000	8mm-10x	<0,001

The same number of iterations was used to test the effect of using α = 3.

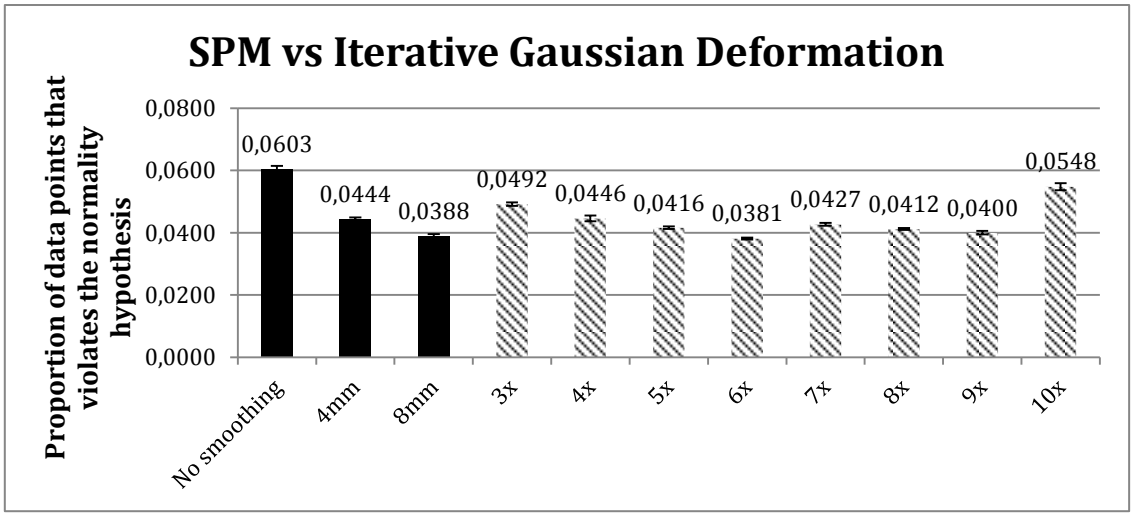

Figure 4.18 - Proportion of data points significantly violating the assumptions of normality with no smoothing, with 4mm and 8mm smoothing (bold) and with iterative Gaussian deformation, using α=3 (striped). The bars represent one standard error.

Table 4.6 - Differences between the groups (no smoothing, 4mm and 8mm and Gaussian deformation for n=3, 4, 5, 6, 7, 8, 9 and 10), given by the p-value of the pairwise comparisons (post hoc with Bonferroni correction).

Kruskal - Wallis			
Sample1 – Sample2	**p-value**	**Sample1 – Sample2**	**p-value**
No smoothing - 3x	1,000	4mm-7x	1,000
No smoothing - 4x	0,024	4mm-8x	1,000
No smoothing - 5x	<0,001	4mm-9x	1,000
No smoothing - 6x	<0,001	4mm-10x	0,504
No smoothing - 7x	0,024	8mm-3x	0,024
No smoothing - 8x	<0,001	8mm-4x	1,000
No smoothing - 9x	<0,001	8mm-5x	1,000
No smoothing - 10x	1,000	8mm-6x	1,000
4mm-3x	1,000	8mm-7x	1,000
4mm-4x	1,000	8mm-8x	1,000
4mm-5x	1,000	8mm-9x	1,000
4mm-6x	1,000	8mm-10x	<0,001

The best result while using the scale factor α=1 was found for n=9 (proportion of 0.0404), as seen in Figure 4.17. However, for α=3, the best result was found for n=6 (proportion of 0.0381). Hence, the images obtained with both these specifications were used to find the results in terms of regional distribution of non-normality as well as for the VBM analysis.

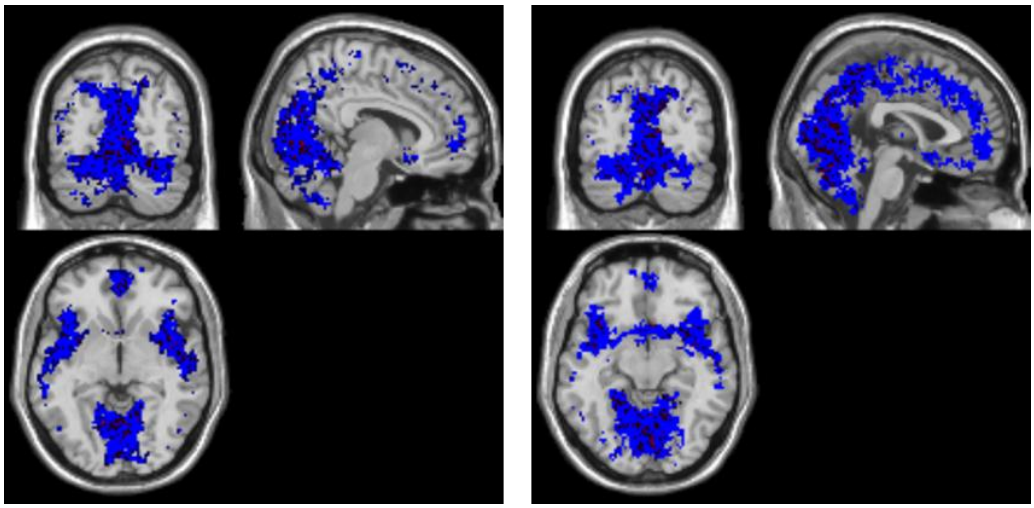

Figure 4.19 - Representation of the regional distribution of non-normal voxels (red) for the images smoothed with the iterative deformation method, for iterations n=9 with α=1 (left) and n=6 with α=3 (right). The blue regions represent the regions that were considered in the analysis.

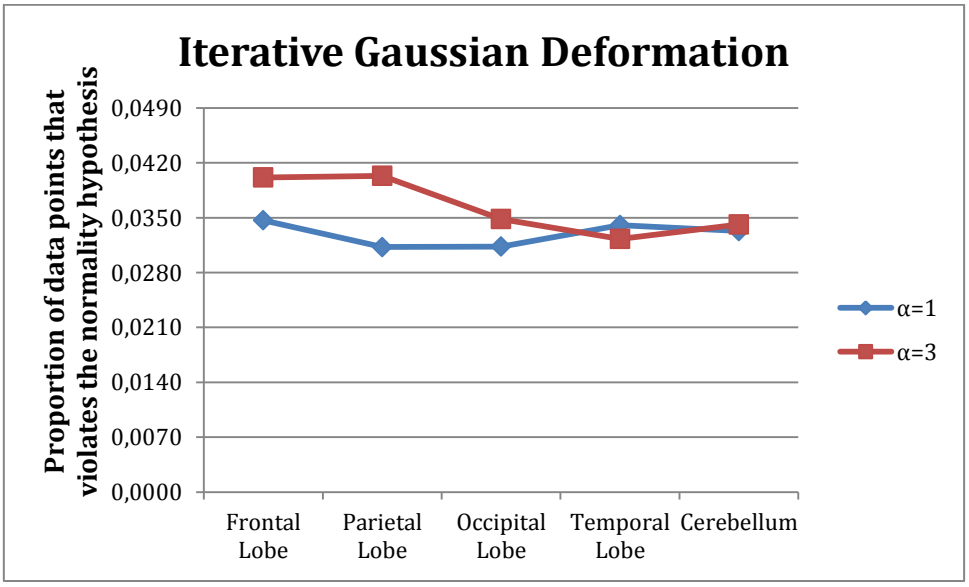

Figure 4.20 - Regional proportion of non-normal voxels for the images smoothed with the iterative Gaussian deformation method, for iterations n=9 with α=1 (blue) and n=6 with α=3 (red).

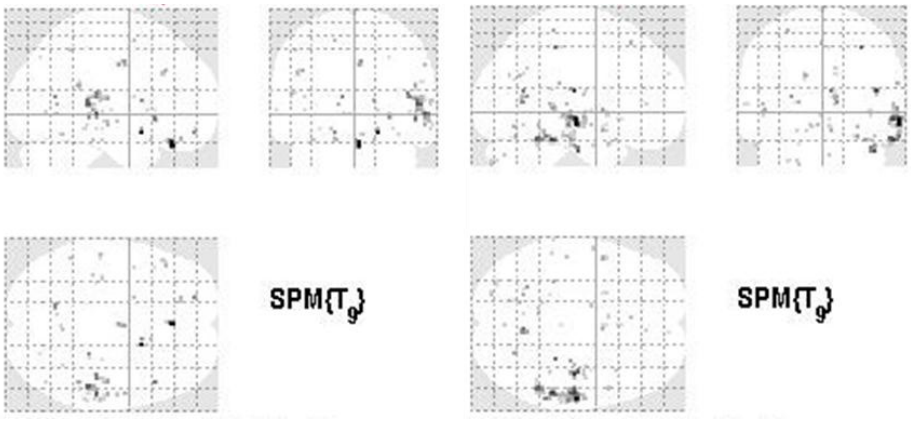

Figure 4.21 - Statistical parametric map resulting of the VBM analysis of the images smoothed with the iterative Gaussian deformation method, for iterations n=9 with α=1 (left) and n=6 with α=3 (right).

Chapter 5

5 DISCUSSION AND CONCLUSIONS

5.1 Objectives

This thesis had the following objectives:

i) implement a method for the assessment of the normality of the data, both globally and by mapping out locations of "difficult" Gaussianization;

ii) develop and assess alternative methods of Gaussianization that could address the drawbacks of the smoothing method currently used, comparing these to the standard approach; and

iii) visually assess the resulting statistical maps to evaluate anatomical accuracy gains, if any.

It can be stated that all the goals of these work have been accomplished. The methods developed both for assessment of normality and Gaussianization can be seen in Chapter 3. The visual assessment of the resulting statistical maps of all the methods, both standard and developed, is present in Chapter 4.

A brief discussion of the results, as well as some conclusions and suggestions for future work are presented below.

5.2 Gaussianization

According to the results shown in Chapter 4, the developed Gaussianization methods can, in fact, render the data more normally distributed as compared to the standard SPM methods. Apart from the underwhelming results from the histogram equalization approach, which will not be further mentioned, the novel solutions

presented here were effective. In effect, at least in mathematical terms, it can be said that the developed methods are by and large not inferior to Gaussian kernel convolution approaches currently in use.

However, looking at the figures representing the regional distribution of the non-normal voxels, it can be seen that there is a spatial issue that affects the analysis: in fact, there is a trade-off between the Gaussianization methods and the number of voxels used in the analysis. This trade-off is originated by the use of relative masking to threshold the image analysis: this masking ensures that only voxels with a high probability of being grey matter in most subjects analysed are actually included in the model. As such, voxels where registration is less adequate and/or where there is a great discrepancy between subjects are discarded. What was observed was that this threshold method is heavily biased towards the more traditional smoothing methods: in the latter, segments are so heavily blurred that inter-subject consistency is ensured by the simple fact that all voxels become fairly homogeneous; this rewards the loss of anatomical accuracy and penalizes methods where accuracy is more preserved, as observed.

Notice the case of the standard smoothing: the Gaussianization is performed by a smoothing step, as seen in Section 3.1, which blurs the image while compensating for the inaccuracies occurred in the registration step – this means that, during the statistical analysis, more voxels are included.

In the case of the Gaussian Deformation method (especially in the iterative Gaussian deformation), the "blurring" effect is attenuated, resulting in a relative mask with a smaller number of voxels (Figure 4.13 and Figure 4.19).

Lastly, in the logit transform method, the transformation of the image is done differently: only the intensity values of the images are being altered, but the structure of the image remains. Thereby, this method does not compensate the registration step or any inhomogeneity and, consequently, many non GM voxels are detected. Thus, the number of voxels used in the relative mask is very low, as it can be seen in Figure 4.7.

5.3 Visual Assessment with VBM

In the Section 5.2, it was noted that the developed Gaussianization methods has the ability to render the data more normally distributed. However, it is necessary to ensure that these methods also enable an accurate detection of significant differences in the GM volume between groups. Therefore, it is important to evaluate possible accuracy gains. This can be achieved through visual assessment of the statistical maps resulting from the VBM analysis.

Notice Figure 4.9, concerning the logit transformation method. The image shows a noisier signal when compared to the standard smoothing, albeit more specific. However, as referred in Section 5.2, the number of voxels used in the statistical analysis is very small; thus, this method is prone to false negatives and cannot be recommended.

Regarding the Gaussian deformation method, signals are also noisier relative to the standard smoothing. Nevertheless, these signals are also more accurate, i.e. the regions where there are significant differences in the GM volume between groups are better defined and are likely true positives (given the knowledge of the ground truth). Hence, it can be said that these methods can, in fact, provide anatomical accuracy gains, when compared to the standard method. The detected regions are, however, less contiguous: this is expected due to the naturally variable anatomy of the subjects, which cannot be fully accounted for by the registration method.

5.4 Limitations and Future work

This works presents with several limitations that must be acknowledged. As immediate factor that stands out from the discussion above is the evaluation of the impact of these Gaussianization methods using threshold masking in the analyses. Other options exist in SPM, notably no masking or absolute threshold masking: it would be sensible to assess the impact of the developed methods on both cases, which can be done in future work. Another important limitation lies in the form of

assessing the preservation of anatomical “accuracy”: whereas this was done visually, which is in fact important in practical terms, future work should attempt to quantify this within a metric that can be objectively measured. Also, the small number of subjects used in both assessing the residuals of the GLM, and then the regional and visual impact of the methods, may have been detrimental to the inferential capability of the analyses performed. Additionally, the dependent variables used in the GLM in the analysis of the residuals should have been more thoroughly tested. Finally, it must be pointed out that the histogram equalization approach, which failed to present any benefit, was designed to achieve uniform distributions rather than Gaussian distributions, which may explain its poor performance. All these points should be addressed in a follow up to this work.

References

[1] “Brain Imaging,” Neuromedia Corner, [Online]. Available: http://www.neuromedia.eu/Sections.aspx?section=21.24. [Accessed 2 July 2014].

[2] R. A. Poldrack, “Region of interest analysis for fMRI,” *Social Cognitive and Affective Neuroscience,* vol. 2, no. 1, pp. 67-70, 2007.

[3] J. L. Whitwell, “Voxel-Based Morphometry: An Automated Technique for Assessing Structural Changes in the Brain,” *The Journal of Neuroscience,* vol. 29, no. 31, p. 9661–9664, 2009.

[4] L. K. Parks, D. E. Hill, R. J. Thoma, M. J. Euler, J. D. Lewine and R. A. Yeo, “Neural correlates of communication skill and symptom severity in autism: A voxel-based morphometry study,” *Research in Autism Spectrum Disorders,* vol. 3, no. 2, pp. 444-454, 2009.

[5] J. Ashburner and K. J. Friston, “Voxel-Based Morphometry—The Methods,” *NeuroImage,* vol. 11, no. 6 Pt 1, pp. 805-21, 2000.

[6] A. Connelly, C. Salmond, D. Gadian, F. Vargha-Khadem, J. Ashburner and K. J. Friston, “Distributional Assumptions in Voxel-Based Morphometry,” *NeuroImage,* vol. 17, no. 2, pp. 1027-1030, 2002.

[7] R. Pohmann, “Physical Basics of NMR,” in *In Vivo NMR Imaging*, vol. 771, Springer Science+Business Media, 2011, pp. 3-21.

[8] H. Panepucci, “Magnetic Ressonance Imaging - Tutorial I,” São Paulo, 1994.

[9] D. Hoa, “Nuclear Magnetic Resonance,” IMAIOS SAS, [Online]. Available: http://www.imaios.com/en/e-Courses/e-MRI/NMR. [Accessed 30 April 2014].

[10] J. Pereira, *Characterisation, Optimisation and Application of Voxel Based Morphometry in MRI Studies of Dementia,* P.h. D. Thesis, Cambridge University, U.K., 2010.

[11] H. M. Lee, J. H. Kim, J.-W. Jang, K.-Y. Kwon, M.-J. Kim, S.-I. Suh and S.-B. Koh, “Subcortical grey matter changes in untreated, early stage Parkinson's disease without dementia.,” *Parkinsonism & related disorders,* vol. 3, no. 6, pp. 622-6, 2014.

[12] A. Tungkasthan and W. Premchaiswadi, “Automatic region of interest detection in natural images,” in *15th World Scientific and Engineering Academy and Society (WSEAS) International Conference on Computers*, Wisconsin, USA, 2011.

[13] “Structural Brain Mapping Group,” [Online]. Available: http://dbm.neuro.uni-

jena.de/vbm/segmentation/modulation/. [Accessed 27 May 2014].

[14] F. K. Ashburner J, “Unified segmentation,” *Neuroimage,* no. 26, p. 839–851, 2005.

[15] D. W. Wichern and R. A. Johnson, Applied Multivariate Statistical Analysis, New Jersey: Pearson Education, Inc., 2007.

[16] A. Heinz, M. Slifstein, M. Reimold, R. Bares and W. Mueller-Schauenburg, “Effect of spatial smoothing on t-maps: arguments for going back from t-maps to masked contrast images.,” *Journal of cerebral blood flow and metabolism : official journal of the International Society of Cerebral Blood Flow and Metabolism,* vol. 26, no. 6, pp. 751-9, 2005.

[17] A. Mechelli, C. J. Price, K. J. Friston and J. Ashberner, “Voxel-Based Morphometry Applications of the Human Brain : Methods and Applications,” *Current Medical Imaging Reviews,* vol. 1, pp. 1-9, 2005.

[18] C. Taylor, “What is a histogram?,” About.com statistics, [Online]. Available: http://statistics.about.com/od/HelpandTutorials/a/What-Is-A-Histogram.htm. [Accessed 5 June 2014].

[19] R. C. Gonzalez and R. E. Woods, Digital Image Processing, New Jersey: Pearson Education, Inc., 2002.

[20] “Central Limit Theorem,” WolframMathWorld, [Online]. Available: http://mathworld.wolfram.com/CentralLimitTheorem.html. [Accessed 25 June 2014].